https://doi.org/10.5194/egusphere-2026-6542
Preprint. Discussion started: 10 November 2026
© Author(s) 2026. CC BY 4.0 License.

Sideband asymmetry determines the information loss of double-sideband detection in submillimetre-wave atmospheric sounding

Ryosuke Tamura[1], Kentaro Araki[2], and Nawo Eguchi[3]

[1] Sensor System Research Group, Research and Development Directorate, Japan Aerospace Exploration Agency, Tsukuba, Ibaraki 305-8505, Japan
[2] Department of Typhoon and Severe Weather Research, Meteorological Research Institute, Japan Meteorological Agency, Tsukuba, Ibaraki 305-0052, Japan
[3] Centre for Oceanic and Atmospheric Research, Research Institute for Applied Mechanics, Kyushu University, Kasuga, Fukuoka 816-8580, Japan

Correspondence to: Ryosuke Tamura (tamura.ryohsuke@jaxa.jp)

Abstract.

Microwave and submillimetre radiometric sounders usually use double-sideband (DSB) detection, which down-converts the lower sideband (LSB) and the upper sideband (USB) flanking the local-oscillator frequency into a single intermediate-frequency channel. If the two sidebands have identical observation sensitivities (Jacobians), this superposition loses no information; where a nearby absorption line makes the Jacobians differ, the information in their difference is lost. We quantify this loss relative to direct detection (DD), which samples the corresponding lower- and higher-frequency RF bands independently. With the system noise temperature, the integration time and the total detected radio-frequency bandwidth matched, we show analytically that the difference between the two schemes' inverse retrieval error covariance matrices is positive semi-definite: the retrieval error variance of DD never exceeds that of DSB. We then evaluate the degrees of freedom for signal (DOFS) and the retrieval errors of temperature, water vapour and relative humidity at 118.75, 183.31, 325.15, 368.49 and 380.20 GHz with ARTS and the FASCODE standard atmospheres. In four of these bands the Jacobians are nearly symmetric and the loss is negligible. At the 368.49 GHz oxygen band, by contrast, the 380.20 GHz water-vapour line 12 GHz above it makes them asymmetric: the DOFS ratio falls with intermediate frequency, reaching 0.50–0.55 at 10 GHz, and the DSB retrieval errors of temperature, water vapour and relative humidity exceed those of DD between 2 and 10 km; over 0–5 km the DSB scheme retains only 27–39 % of the DD degrees of freedom in the tropical atmosphere. Under the adopted prior, channel and noise assumptions, the DD advantage there persists until its system noise temperature exceeds that of DSB by a factor of about 2.2–2.4 for temperature and for tropical water vapour, but only about 1.3 for subarctic-winter water vapour, providing a quantitative basis for choosing the detection scheme of submillimetre sounders.

1 Introduction

The vertical distributions of temperature and water vapour are important for numerical weather prediction, climate monitoring and the understanding of dynamical processes in the atmosphere. Passive

https://doi.org/10.5194/egusphere-2026-6542
Preprint. Discussion started: 10 November 2026
© Author(s) 2026. CC BY 4.0 License.

sounders in the microwave and submillimetre range provide global vertical information by day and by night, and operational sounders such as AMSU-A (Mo, 1996) and ATMS (Weng et al., 2012) are regarded as among the observing systems with the largest observation impact in numerical weather prediction (Eyre et al., 2022).

Radiometric sounding exploits the fact that the effective emission height varies with the frequency offset from an absorption line centre. In the troposphere the line width is roughly proportional to pressure through pressure broadening, so that channels close to the line centre sense the upper atmosphere and channels in the line wings sense the lower atmosphere (Janssen, 1993; Ulaby and Long, 2014). The oxygen bands at 60 and 118.75 GHz have been used to retrieve temperature and the 183.31 GHz water-vapour line to retrieve water vapour, but in recent years observations have extended into the submillimetre range, including the water-vapour lines at 325.15 and 380.20 GHz and the oxygen line at 368.49 GHz (Buehler et al., 2007), with flown and planned instruments such as SMILES (Kikuchi et al., 2010), the airborne ISMAR (Fox et al., 2017) and ICI on MetOp-SG (Buehler et al., 2012; Eriksson et al., 2020).

The submillimetre spectrum is formed by the overlap of numerous absorption lines and the water-vapour continuum (Rosenkranz, 1998; Mlawer et al., 2012), so that the brightness temperature and the temperature and water-vapour Jacobians can be asymmetric about a line centre. The oxygen line at 368.49 GHz is a particular case: the strong water-vapour line at 380.20 GHz lies about 12 GHz above it, so that the vertical distribution of sensitivity differs substantially between the low- and high-frequency sides of the line centre.

Receivers in the microwave and submillimetre range widely use heterodyne detection with frequency conversion, and double-sideband (DSB) detection, which dispenses with the sideband filter ahead of the mixer, has become the standard configuration (Janssen, 1993; Goldsmith, 1998). In the DSB scheme the signals of the lower sideband (LSB) and the upper sideband (USB), which lie on either side of the local-oscillator frequency, are superposed in a single intermediate-frequency channel and detected together, so that no information is lost if the two Jacobians coincide, whereas if they are asymmetric the independent information contained in their difference is lost in principle. Single-sideband (SSB) detection and sideband-separating receivers avoid the superposition, but at the cost of the loss and the complexity that come with implementing filters or separating circuits (Kikuchi et al., 2010).

Meanwhile, the extension of semiconductor low-noise amplifiers (LNAs) to higher frequencies, which has advanced markedly in recent years, is making direct-detection (DD) receivers — in which the signal is amplified and then detected without frequency conversion — a practical and promising option up to the 300 GHz range, including for small-satellite missions (Tessmann et al., 2017). Its extension to the 368–380 GHz range considered here has yet to be demonstrated, and DD is therefore treated in this study as a conceptual receiver architecture. Because the observation channels of a DD receiver can be placed independently on the low- and high-frequency sides of an absorption line, DD has the essential advantage that the superposition of the LSB and the USB that characterises DSB detection does not arise in the first place.

https://doi.org/10.5194/egusphere-2026-6542
Preprint. Discussion started: 10 November 2026
© Author(s) 2026. CC BY 4.0 License.

The superposition of the LSB and the USB itself has long been recognised in the radiometer and heterodyne receiver communities. In receiver engineering the sensitivity (system noise temperature) of SSB and DSB detection has been compared, mainly in the context of radio astronomy (Penzias and Burrus, 1973); in spectroscopic radio astronomy, sideband deconvolution techniques have been developed that recover a single-sideband spectrum from the spectrum folded by DSB detection (Comito and Schilke, 2002). In atmospheric limb observation, the sideband ratio has been treated as a calibration quantity and as a parameter of the forward model (Barath et al., 1993). Information-content analyses of submillimetre sounder channels, including the sideband-paired channels of ICI, have likewise taken the double-sideband channel definitions as given (Grützun et al., 2018).

All of these studies, however, were aimed at comparing receiver sensitivities, at recovering spectra, or at refining forward models, and none of them asks how the superposition of the LSB and the USB affects the retrieval accuracy of the atmospheric state variables themselves. The classical sounding bands (the oxygen absorption complex near 60 GHz and the 118.75 GHz oxygen line, and the water-vapour lines at 22.235 and 183.31 GHz) are almost symmetric about the line centre over the range of intermediate frequencies actually used, and, as shown below, the information loss is exactly zero when the Jacobians coincide. The question acquires substance only once the observations extend into the submillimetre range, where neighbouring absorption lines and the water-vapour continuum break that symmetry. Indeed, to the best of the authors' knowledge, no study has quantified the effect of the information loss due to the superposition of the LSB and the USB on the DOFS and the retrieval error of atmospheric sounding under an idealised comparison in which the system noise temperature, the integration time and the total RF bandwidth are matched.

The aim of this study is to quantify the information loss due to DSB detection and thereby to provide a quantitative criterion for the choice of detection scheme in submillimetre sounders. To that end we first derive theoretically the difference between the inverse retrieval error covariance matrices of the DD and DSB schemes, and show analytically that DD is always superior or equivalent to DSB in statistical precision. We then apply a MAP error analysis, using ARTS (Eriksson et al., 2011; Buehler et al., 2025) and the FASCODE standard atmospheres (Smith et al., 1978), to the five bands at 118.75, 183.31, 325.15, 368.49 and 380.20 GHz, and identify the conditions under which the information loss due to DSB detection is negligible and those under which the LSB and the USB must be preserved independently.

2 Data and Methods

2.1 Atmospheric profile data

Five standard atmospheric profiles defined in the Fast Atmospheric Signature Code (FASCODE) were used: tropical, midlatitude winter, midlatitude summer, subarctic winter and subarctic summer (Smith et al., 1978). The pressure, temperature, altitude, water-vapour volume mixing ratio (VMR) and ozone VMR

https://doi.org/10.5194/egusphere-2026-6542
Preprint. Discussion started: 10 November 2026
© Author(s) 2026. CC BY 4.0 License.

defined for each profile were used as input to the Atmospheric Radiative Transfer Simulator (ARTS) for the radiative transfer calculations (Buehler et al., 2025).

This study focuses on the 0–10 km altitude range, where the retrieval of vertical temperature and water-vapour profiles by submillimetre sounding is expected to be useful. Comparing the five standard atmospheric profiles, the tropical and subarctic-winter atmospheres show contrasting characteristics in temperature, water-vapour VMR and relative humidity (RH) (Figure 1). In this altitude range the temperature is highest in the tropical atmosphere and lowest in the subarctic-winter atmosphere, and the water-vapour VMR is likewise highest in the tropical and lowest in the subarctic-winter atmosphere. This indicates that the absolute amount of water vapour contained in the atmosphere is large in the tropics and small in the subarctic winter.

The RH, by contrast, tends to be high in the subarctic-winter atmosphere and low in the tropical and midlatitude-summer atmospheres. The RH is the ratio of the water-vapour partial pressure to the saturation vapour pressure, and the saturation vapour pressure decreases as the temperature falls. The RH can therefore be high even in the subarctic-winter atmosphere, where the water-vapour VMR is small, because the low temperature reduces the saturation vapour pressure. This comparison shows that the tropical and subarctic-winter atmospheres are contrasting in temperature, in water-vapour VMR and in RH alike. These two profiles were therefore chosen for the evaluation of the degrees of freedom and of the retrieval accuracy in this study.

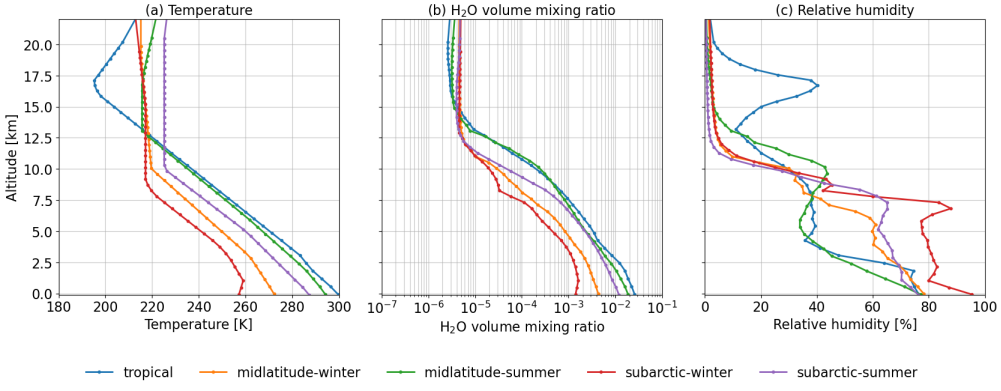


Figure 1(a) Temperature, (b) H_2O volume mixing ratio, and (c) relative humidity for each atmospheric profile. The blue, orange, green, red, and purple lines show the tropical, midlatitude-winter, midlatitude-summer, subarctic-winter, and subarctic-summer atmospheric profiles, respectively.

2.2 Spectral characteristics of brightness temperature and atmospheric absorption

The radiative transfer calculations with ARTS assume satellite observation from space and were set up for nadir viewing in a clear-sky atmosphere. The finite width of the antenna beam was not taken into account, and the brightness temperature was calculated for a single vertically downward line of sight. The

https://doi.org/10.5194/egusphere-2026-6542
Preprint. Discussion started: 10 November 2026
© Author(s) 2026. CC BY 4.0 License.

surface was assumed to be a blackbody with an emissivity of unity and its temperature to be known, so that uncertainties in the surface temperature and the surface emissivity were not considered. Under these conditions, each of the five FASCODE standard profiles was used in turn to calculate the brightness temperature spectrum over 100-400 GHz (Figure 2).

This frequency range contains the oxygen (O2) lines at 118.750 and 368.498 GHz and the water-vapour (H2O) lines at 183.310, 325.153 and 380.197 GHz. Near the centres of these strong lines the optical depth of the atmosphere is large, so the effective emission height of the observed radiation rises. The radiation observed then originates mainly in the colder air aloft, and the brightness temperature falls near the line centre.

In the window regions away from the line centres, by contrast, the brightness temperature decreases gradually with increasing frequency, to a degree that depends on the atmospheric profile. This is mainly because the contribution of the water-vapour continuum grows towards higher frequencies, so that the radiation from the surface and the lower atmosphere is more strongly attenuated. Of the five profiles, the subarctic-winter atmosphere, which has the least water vapour, is relatively little affected by water-vapour absorption and shows a flatter brightness temperature spectrum than the others.

These features of the brightness temperature spectrum can be explained by the frequency dependence of the atmospheric optical depth. For the subarctic-winter and tropical atmospheres, the optical depth integrated from the top of the atmosphere to the surface is shown separately for water vapour, oxygen, ozone (O3) and their sum (Figure 3). Because the volume fraction of oxygen is almost constant throughout the atmosphere, the optical depths of the oxygen lines at 118.75 and 368.49 GHz differ little between the two atmospheres. The optical depth due to the H_2O lines and the water-vapour continuum, on the other hand, reflects the amount of water vapour and is more than an order of magnitude larger in the tropical than in the subarctic-winter atmosphere. In the window regions in particular, the total optical depth of the tropical atmosphere exceeds unity at the higher frequencies, whereas that of the subarctic-winter atmosphere remains around 0.1. This difference corresponds to the degree of the gradual decrease in brightness temperature in the window regions, and to the flatness of the spectrum of the subarctic-winter atmosphere. Although ozone has many absorption lines, their optical depth is small compared with the total at most frequencies, and they appear only as spike-like decreases in brightness temperature in the window regions of the spectrum. These features are also confirmed by the altitude dependence of the absorption coefficient described next.

For the subarctic-winter and tropical atmospheres, the frequency dependence of the absorption coefficient at three altitudes within the troposphere is shown separately by species (Figure 4, Figure 5). Because the tropopause height differs greatly between the two atmospheres, the altitudes selected also differ: 8.00, 4.14 and 2.06 km for the subarctic-winter atmosphere and 14.57, 10.94 and 4.68 km for the tropical atmosphere. These are the altitudes of the levels of the pressure grid used in the radiative transfer calculations and are quoted without rounding. In both atmospheres, the higher the altitude and the lower the pressure, the smaller the pressure broadening and the narrower the absorption lines that appear. At the lowest altitude, by contrast, pressure broadening widens the line wings and the spectrum becomes smooth.

https://doi.org/10.5194/egusphere-2026-6542
Preprint. Discussion started: 10 November 2026
© Author(s) 2026. CC BY 4.0 License.

By species, the contribution of ozone is relatively large at the highest altitude (Figure 4a, Figure 5a), and there are frequencies in the window regions at which the total absorption coefficient is almost entirely set by ozone lines, whereas at the lowest altitude (Figure 4c, Figure 5c) the ozone contribution is several orders of magnitude smaller than that of the other species and is negligible. This is consistent with the interpretation given above that the spike-like decreases in brightness temperature in Figure 2 originate mainly in stratospheric ozone. In the window regions at the lowest altitude, moreover, water-vapour absorption (lines and continuum) is dominant, and its absorption coefficient is about an order of magnitude larger in the tropical than in the subarctic-winter atmosphere. Note that this comparison is made at the same geometric altitude, at which the pressures of the two atmospheres differ. This difference in water-vapour absorption between the atmospheres is the cause of the difference in optical depth and hence of the difference between the brightness temperature spectra.

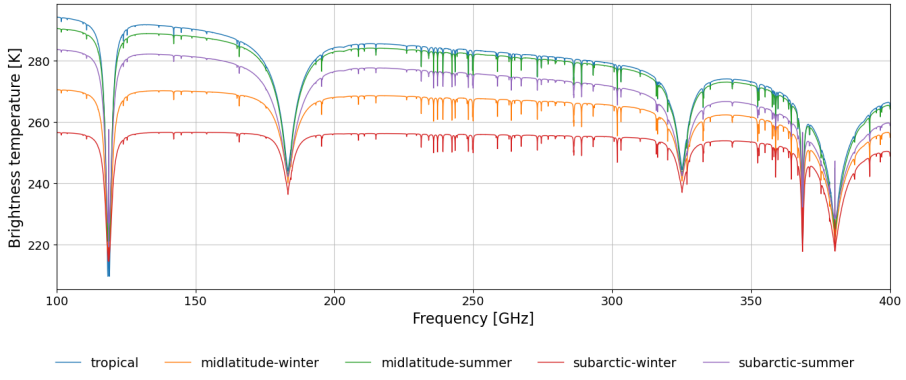


Figure 2 Brightness temperature spectra computed for each atmospheric profile over 100–400 GHz. The radiative transfer calculations assume nadir-viewing observations from a satellite, with the surface treated as a blackbody. The blue, orange, green, red, and purple lines show the tropical, midlatitude-winter, midlatitude-summer, subarctic-winter, and subarctic-summer atmospheric profiles, respectively.

https://doi.org/10.5194/egusphere-2026-6542
Preprint. Discussion started: 10 November 2026
© Author(s) 2026. CC BY 4.0 License.

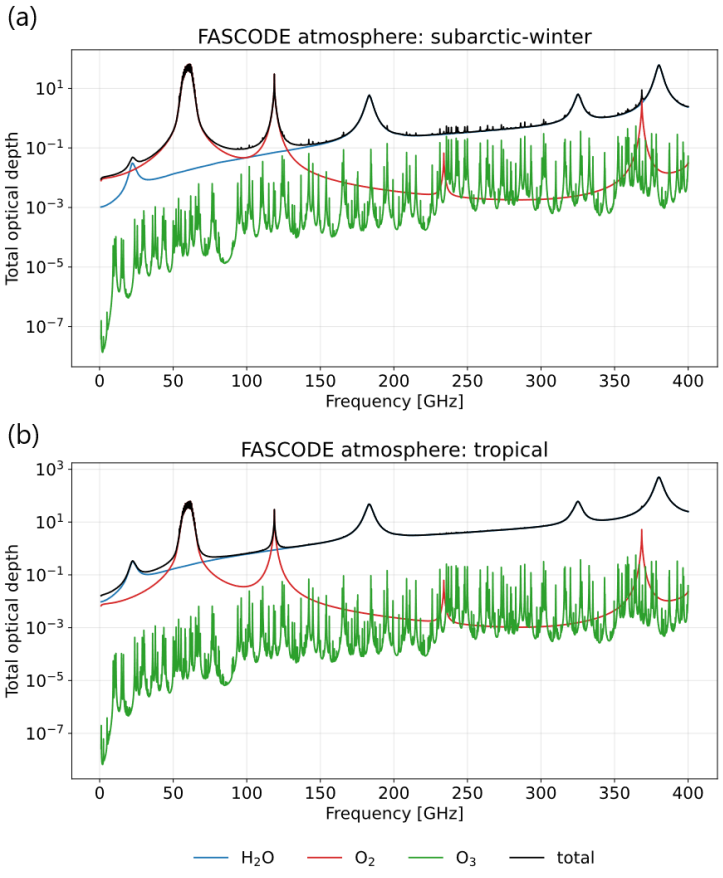


Figure 3 Total optical depth, vertically integrated from the top of the atmosphere to the surface, as a function of frequency. (a) Subarctic-winter atmosphere, (b) tropical atmosphere. The blue, red, and green lines show the optical depth due to water vapour, oxygen, and ozone, respectively, and the black line shows the total optical depth summing these components.

https://doi.org/10.5194/egusphere-2026-6542
Preprint. Discussion started: 10 November 2026
© Author(s) 2026. CC BY 4.0 License.

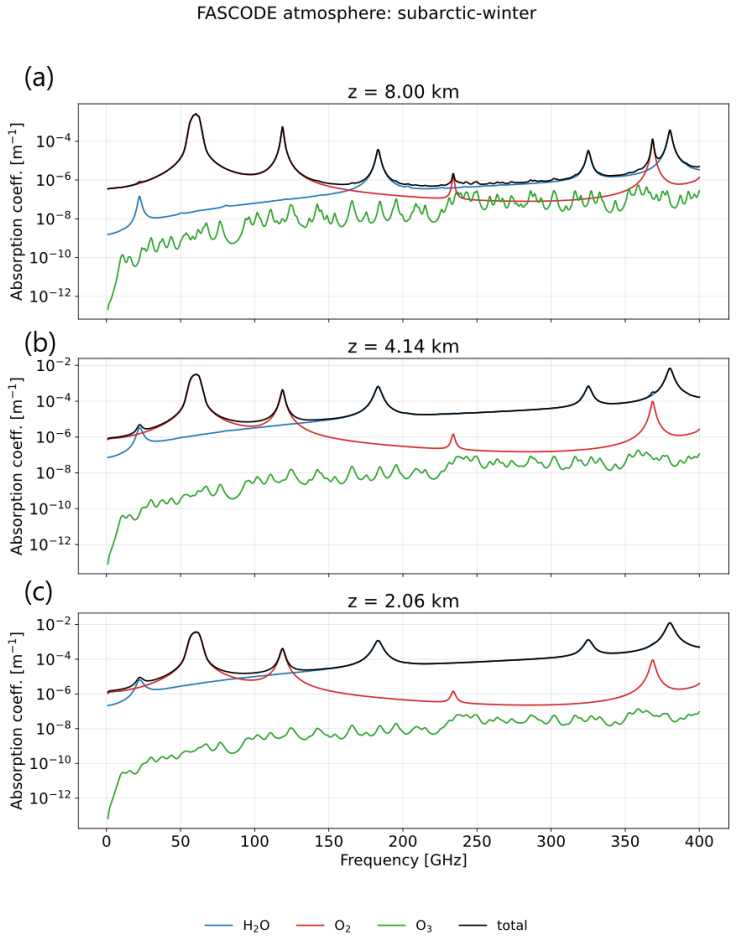


Figure 4 Frequency dependence of the absorption coefficient in the subarctic-winter atmosphere. (a) 8.00 km, (b) 4.14 km, (c) 2.06 km. The blue, red, and green lines show the absorption coefficient due to water vapour, oxygen, and ozone, respectively, and the black line shows their sum.

https://doi.org/10.5194/egusphere-2026-6542
Preprint. Discussion started: 10 November 2026
© Author(s) 2026. CC BY 4.0 License.

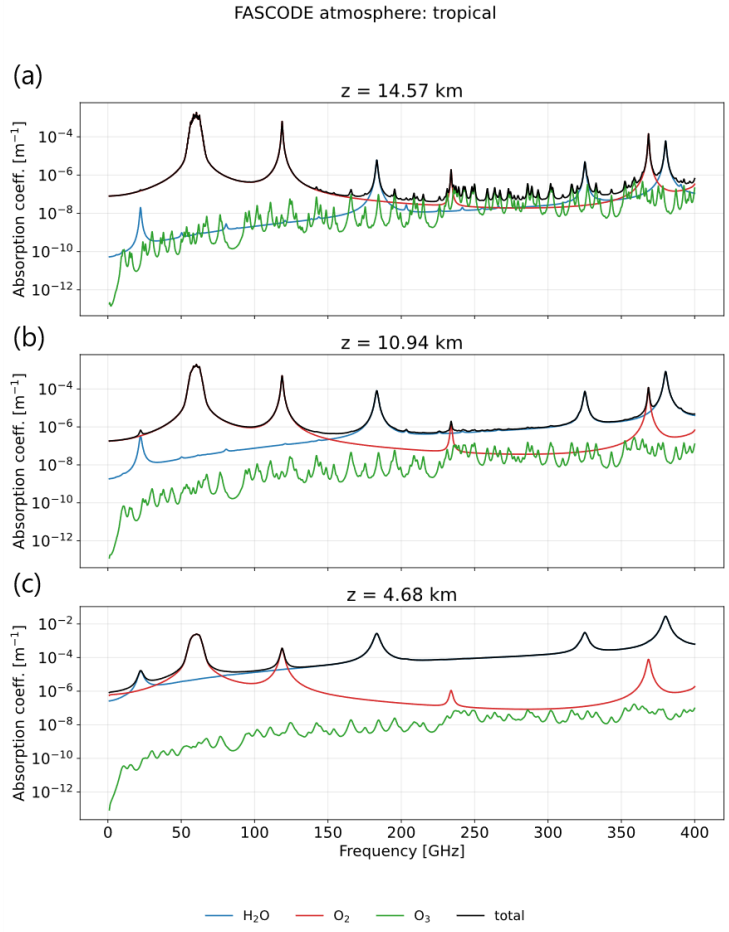


Figure 5 Frequency dependence of the absorption coefficient in the tropical atmosphere. (a) 14.57 km, (b) 10.94 km, (c) 4.68 km. The blue, red, and green lines show the absorption coefficient due to water vapour, oxygen, and ozone, respectively, and the black line shows their sum.

2.3 Retrieval and the degrees of freedom for signal

In this study the information content and the retrieval precision of the vertical distributions of temperature and water vapour obtainable from the observed brightness temperatures were evaluated on the basis of maximum a posteriori (MAP) estimation. MAP estimation combines, through Bayes' theorem, prior information on the atmospheric state such as temperature and water vapour with the observational information that expresses the consistency between the values computed with a radiative transfer model and the observed values (Rodgers, 2000). Writing the observed brightness temperature vector as y and the state vector to be retrieved as x, the observation equation is

https://doi.org/10.5194/egusphere-2026-6542
Preprint. Discussion started: 10 November 2026
© Author(s) 2026. CC BY 4.0 License.

$$y = F(x) + \varepsilon, \tag{1}$$

where F is the radiative transfer model that computes the observed brightness temperature from the state vector and ε is the observation error. Assuming that the state vector and the observation error follow Gaussian distributions, the MAP estimate is obtained by minimising the following cost function.

$$J(x) = [y - F(x)]^{\mathrm{T}} S_{\varepsilon}^{-1} [y - F(x)] + (x - x_a)^{\mathrm{T}} S_a^{-1} (x - x_a), \tag{2}$$

Here x_a is the prior state vector, S_a the prior error covariance matrix and S_ε the observation error covariance matrix. The first term represents the residual between the calculated and the observed brightness temperature and the second the departure of the estimate from the prior state. In MAP estimation the state vector is thus determined by taking account of both the observational and the prior information.

Linearising the radiative transfer model about a reference atmospheric profile, the retrieval error covariance matrix after MAP estimation is given by

$$\hat{S} = (K^{\mathrm{T}} S_{\varepsilon}^{-1} K + S_a^{-1})^{-1}, \tag{3}$$

where

$$K = \frac{\partial F}{\partial x} \tag{4}$$

is the Jacobian matrix representing the sensitivity of the observed brightness temperature to the state vector. For the brightness temperature of each observation channel we computed the Jacobians with respect to temperature and water-vapour VMR using the Jacobian calculation facility implemented in ARTS. The Jacobians with respect to temperature and to water-vapour VMR are defined as follows.

$$K_T = \frac{\partial y}{\partial T}, \; K_q = \frac{\partial y}{\partial q} \tag{5}$$

Here T and q denote the vertical profiles of temperature and water-vapour VMR, respectively. Altitude, ozone VMR and the other atmospheric constituents were fixed at the values given in the FASCODE standard profiles and were not included in the retrieval.

In actual atmospheric sounding, temperature and water vapour both affect the same observed brightness temperature. To include this cross-sensitivity in the analysis, a joint retrieval with a state vector combining temperature and water-vapour VMR was used throughout. The state vector and the Jacobian matrix used in the joint retrieval were defined as

$$x = \begin{bmatrix} T \\ q \end{bmatrix},$$

$$K = [K_T \quad K_q]. \tag{6}$$

We assumed the prior errors of temperature and water vapour to be mutually uncorrelated and set the prior error covariance matrix as the following block-diagonal matrix. The vertical correlation within each block is described in Section 2.6.

$$S_a = \begin{bmatrix} S_{a,TT} & 0 \\ 0 & S_{a,qq} \end{bmatrix} \tag{7}$$

Under this assumption the prior error cross-covariance between temperature and water vapour is not taken into account. By including the Jacobians for temperature and for water vapour in a single state

https://doi.org/10.5194/egusphere-2026-6542
Preprint. Discussion started: 10 November 2026
© Author(s) 2026. CC BY 4.0 License.

vector, however, the cross-sensitivity of the two quantities through the observation is retained in the analysis.

Partitioning the retrieval error covariance matrix obtained from Eq. (3) into the blocks corresponding to temperature and water vapour, it is written as

$$\hat{S} = \begin{bmatrix} \hat{S}_{TT} & \hat{S}_{Tq} \\ \hat{S}_{qT} & \hat{S}_{qq} \end{bmatrix} \tag{8}$$

As a measure of how much the observation contributes to the estimate of the state vector we used the averaging kernel matrix

$$A = I - \hat{S}S_a^{-1} = \hat{S}K^{\mathrm{T}}S_\varepsilon^{-1}K \tag{9}$$

where I is the identity matrix. A expresses the response of the estimate to a change in the true state, and tends to $A \to I$ in the limit in which the state is determined by the observation alone and to $A \to O$ in the limit in which no observational information is available. The second form in Eq. (9) shows that A measures the contribution of the observation through the observation term on the right-hand side of Eq. (3).

The degrees of freedom for signal (DOFS) is the trace of A,

$$d_s = \mathrm{tr}(A), \tag{10}$$

as defined by Rodgers (2000). d_s represents the effective number of components of the state vector that are determined by the observation independently of the prior information; writing the dimension of the state vector as n, it takes values in the range $0 \le d_s \le n$. Information-content evaluation based on optimal estimation theory, of which the DOFS is the best known measure, has also been widely applied, for example to channel selection for hyperspectral infrared sounders (Rodgers, 1990; Rabier et al., 2002; Collard, 2007).

Because temperature and water-vapour VMR are retrieved jointly in this study, the averaging kernel matrix was partitioned according to the state vector of Eq. (6) as

$$A = \begin{bmatrix} A_{TT} & A_{Tq} \\ A_{qT} & A_{qq} \end{bmatrix} \tag{11}$$

and the degrees of freedom of temperature and of water-vapour VMR were evaluated as $d_T = \mathrm{tr}(A_{TT})$ and $d_q = \mathrm{tr}(A_{qq})$, respectively. By the additivity of the trace, their sum equals the total degrees of freedom d_s.

In order to establish at which altitudes the information obtained from the observation appears, we further defined a layer-wise DOFS, in which only the diagonal elements belonging to the vertical grid points of a given altitude layer L are summed,

$$d_u(L) = \sum_{i \in L} (A_{uu})_{ii}, \quad u \in \{T, q\}. \tag{12}$$

Here $d_u(L)$ represents the amount of information obtained independently from the observation within that altitude layer, and the sum over all layers equals d_u. In this study the layer-wise DOFS was compared between the DD and DSB schemes for the 0–5 km and 5–10 km layers, which are the principal targets of next-generation sounders (Section 4.1).

https://doi.org/10.5194/egusphere-2026-6542
Preprint. Discussion started: 10 November 2026
© Author(s) 2026. CC BY 4.0 License.

To evaluate the improvement in retrieval precision brought by the observational information at each altitude, the ratio of the retrieval error to the prior error was defined for temperature, water-vapour VMR and RH as follows.

$$R_{u,i} = \frac{\sigma_{u,i}}{\sigma_{a,u,i}},\ u \in \{T, q, RH\} \quad (13)$$

$R_{u,i} = 1$ means that the observation brings no reduction of the error and that the uncertainty of the estimate is dominated by the prior information. $R_{u,i} < 1$, by contrast, means that the prior error has been reduced by the observational information; the smaller the value, the greater the improvement in retrieval precision brought by the observation.

For the DD and DSB schemes we constructed the observation vector, the Jacobian matrix and the observation error covariance matrix appropriate to each detection scheme, and compared the DOFS and the retrieval error under identical prior state and prior error conditions. The information lost by the superposition of the LSB and the USB was quantified as the difference in DOFS and in retrieval error between the DD and DSB schemes.

The retrieval errors computed here are theoretical errors obtained on the assumption that the prior and observation errors follow Gaussian distributions and that the radiative transfer model can be linearised about the reference atmospheric profile. They therefore do not include error sources not treated explicitly in this study, such as uncertainties in the spectroscopic parameters, systematic errors of the radiative transfer model and errors in the surface temperature and surface emissivity.

2.4 Detection schemes and noise conditions

The detection schemes of microwave and submillimetre radiometers fall into two broad classes: heterodyne detection (Figure 6a, b), in which the signal at the observation frequency f_{RF} is mixed with the local-oscillator signal at f_{LO} in a frequency mixer and converted to an intermediate frequency (IF) f_{IF} before detection; and direct detection (Figure 6c), in which the signal at the observation frequency is detected without frequency conversion.

Heterodyne detection is classified into double-sideband (DSB) and single-sideband (SSB) detection according to whether a sideband is selected ahead of the mixer. In the DSB scheme neither sideband is removed ahead of the mixer, so that, from the relation $f_{\mathrm{IF}} = |f_{\mathrm{RF}} - f_{\mathrm{LO}}|$, the two RF signals located at $f_{\mathrm{RF}} = f_{\mathrm{LO}} \pm f_{\mathrm{IF}}$ are converted into the same IF channel and the LSB and USB signals are detected superposed (Figure 6d). In the SSB scheme, by contrast, a low-pass or high-pass filter is placed ahead of the mixer and only the LSB or the USB, defined with respect to f_{LO}, is selected and detected (Figure 6e). In direct detection the RF signal is amplified and detected without frequency conversion, so that the observation channels can be placed independently on the low-frequency and high-frequency sides of the target absorption line (Figure 6f). Note that LSB and USB are named with respect to the local-oscillator frequency, whereas the low-frequency and high-frequency sides used hereafter are named with respect to the line centre.

https://doi.org/10.5194/egusphere-2026-6542
Preprint. Discussion started: 10 November 2026
© Author(s) 2026. CC BY 4.0 License.

Assuming nadir observation from a satellite, we quantify the information loss due to DSB detection in the 100–400 GHz range by comparison with the DD scheme. Because SSB detection selects only the low- or only the high-frequency side of the line centre, it is not suited to the purpose of this study, which is to examine whether the information of the LSB and the USB is retained or lost. The quantitative comparison that follows therefore treats DD and DSB detection, and SSB detection is not included. An idealised comparison of the two schemes, with matched system noise temperature, integration time and total RF bandwidth, requires the relation between the radio-frequency (RF) bandwidth contributing to detection and the observation noise to be taken into account. In what follows we set the noise-equivalent differential temperature (NEDT) of the two schemes from the radiometer equation and set out the relation between the Jacobian matrices and the retrieval error covariance matrices.

The brightness temperature resolution of a radiometer, ΔT, is given by

$$\Delta T = T_{\mathrm{sys}} \left[\frac{1}{B\tau} + \left(\frac{\Delta g_{\mathrm{sys}}}{g_{\mathrm{sys}}} \right)^2 \right]^{1/2} \tag{14}$$

where T_{sys} is the system noise temperature, B the RF bandwidth contributing to the detection, τ the integration time and $\Delta g_{\mathrm{sys}}/g_{\mathrm{sys}}$ the relative fluctuation of the system gain. In this study the gain fluctuation was neglected and $\Delta g_{\mathrm{sys}} = 0$ was assumed. The NEDT is then proportional to T_{sys} and inversely proportional to the square root of the RF bandwidth. Hence, if T_{sys} and τ are the same, the difference in the RF bandwidth contributing to the detection appears as a difference in observation accuracy.

In this study T_{sys} was assumed to be constant, independent of the detection scheme and of the frequency. The antenna, T_{sys} and τ were taken to be identical for the two schemes, and the bandwidth of each IF channel of the DSB scheme and that of each RF channel of the DD scheme were both set to $B = 0.5$ GHz. In the DSB scheme the LSB and the USB, which lie on either side of f_{LO}, are folded into the same IF channel, so that the total RF bandwidth contributing to the detection of one IF channel is $2B = 1.0$ GHz. The RF bandwidth corresponding to one observation channel of the DD scheme, by contrast, is B. The NEDT of the DSB scheme is therefore $1/\sqrt{2}$ times the NEDT of a single channel of the DD scheme.

In this study two DD channels placed symmetrically about the absorption line (Ch1 and Ch2 in Figure 6f) were made to correspond to one DSB channel. The total RF bandwidth contributing to the detection is thereby $2B$ for both schemes.

Let K_{L} and K_{U} be the Jacobian matrices for the LSB and the USB, respectively. In DD detection, which has no local oscillator, the corresponding lower- and higher-frequency RF bands are retained as independent observation channels; for convenience we keep the LSB/USB notation for these bands, so the Jacobian matrix and the observation error covariance matrix are

$$K_{\mathrm{DD}} = \begin{bmatrix} K_{\mathrm{L}} \\ K_{\mathrm{U}} \end{bmatrix}, \; S_{\epsilon,\mathrm{DD}} = \sigma_{\mathrm{DD}}^2 I \tag{15}$$

https://doi.org/10.5194/egusphere-2026-6542
Preprint. Discussion started: 10 November 2026
© Author(s) 2026. CC BY 4.0 License.

In the DSB scheme, in which the gains of the LSB and the USB are equal, the observed brightness temperature and the Jacobian are given by the average of the LSB and the USB, so that

$$K_{\mathrm{DSB}} = \frac{K_{\mathrm{L}}+K_{\mathrm{U}}}{2} \tag{16}$$

Furthermore, since twice the radio-frequency bandwidth of a single DD channel contributes to detection in DSB detection, the observation error variance is

$$\sigma^2_{\mathrm{DSB}} = \frac{\sigma^2_{\mathrm{DD}}}{2}. \tag{17}$$

The theoretical comparison below assumes an ideal DSB scheme with equal LSB and USB gains. It further assumes that the antenna, the system noise temperature, the integration time and the total RF bandwidth are the same for the DD and DSB schemes, and that the frequency response of each observation channel is rectangular. The observation errors are taken to be uncorrelated between channels, and the same prior state and prior error covariance matrix are used for both schemes. We further assume the linear, Gaussian MAP framework of Section 2.3. The ordering of the retrieval error covariance matrices given below holds under these conditions.

When the same prior error covariance matrix is used for the DD and DSB schemes, the prior information term of Eq. (3) cancels and the difference between the inverse retrieval error covariance matrices is determined by the observation term alone. Writing this difference as ΔH and setting $\sigma = \sigma_{\mathrm{DD}}$,

$$\begin{aligned}\Delta H &= \hat{S}^{-1}_{\mathrm{DD}} - \hat{S}^{-1}_{\mathrm{DSB}} \\ &= \boldsymbol{K}^T_{DD}\boldsymbol{S}^{-1}_{\epsilon,DD}\boldsymbol{K}_{DD} - \boldsymbol{K}^T_{DSB}\boldsymbol{S}^{-1}_{\epsilon,DSB}\boldsymbol{K}_{DSB} \\ &= \frac{1}{2\sigma^2}(K_{\mathrm{U}} - K_{\mathrm{L}})^{\mathrm{T}}(K_{\mathrm{U}} - K_{\mathrm{L}})\end{aligned} \tag{18}$$

The right-hand side is a Gram matrix of the form $\mathrm{A}^{\mathrm{T}}\mathrm{A}$ and is therefore symmetric positive semi-definite (that is, its quadratic form is non-negative for any vector), so that

$$\hat{S}^{-1}_{\mathrm{DD}} \succeq \hat{S}^{-1}_{\mathrm{DSB}} \tag{19}$$

holds. Since both retrieval error covariance matrices are positive definite, the order-reversing property of the positive semi-definite ordering gives

$$\hat{S}_{\mathrm{DD}} \preceq \hat{S}_{\mathrm{DSB}} \tag{20}$$

The condition for equality, at which the two retrieval error covariance matrices coincide, is

$$K_{\mathrm{L}} = K_{\mathrm{U}} \tag{21}$$

that is, when the LSB and USB Jacobians coincide. Under the comparison conditions of this study, therefore, the retrieval error variance of each state variable for the DD scheme is no larger than that for the DSB scheme, and the retrieval precision of DD never falls below that of DSB. This is described in detail in Appendix A. When the LSB and USB Jacobians coincide, the retrieval precisions of the two schemes are equal and DSB detection causes no information loss.

https://doi.org/10.5194/egusphere-2026-6542
Preprint. Discussion started: 10 November 2026
© Author(s) 2026. CC BY 4.0 License.

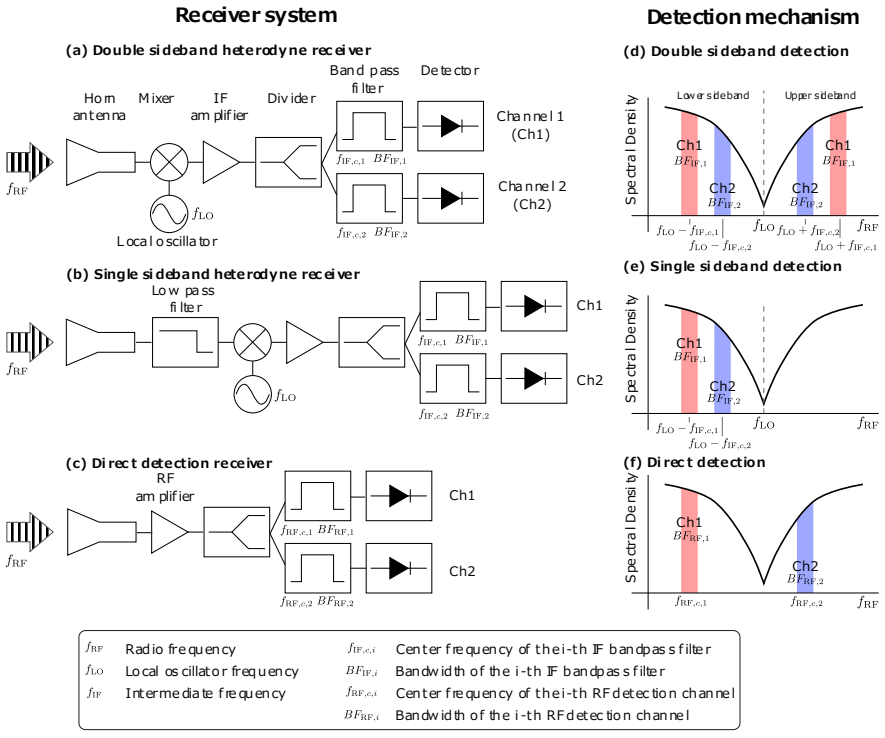


Figure 6 Configuration of the three receiver architectures (left column), and a schematic of the detection scheme on the radio-frequency (RF) spectrum observed by each (right column). (a) Double-sideband (DSB) heterodyne receiver, (b) single-sideband (SSB) heterodyne receiver, (c) direct-detection (DD) receiver. In the heterodyne receivers (a, b), the signal received by the horn antenna is down-converted to the intermediate-frequency (IF) band using the local-oscillator (LO) frequency, and after amplification and splitting, each channel is detected through a bandpass filter and a detector. In the DSB scheme (d), the lower sideband (LSB) and upper sideband (USB), which lie symmetrically about the LO frequency, are superimposed onto the same IF channel, so each channel (Ch1, Ch2) receives contributions from both the LSB and the USB simultaneously. In the SSB scheme (e), a low-pass filter retains only one sideband, while the other sideband (the channel shown with a dashed outline) is rejected. In the direct-detection scheme (f), no frequency conversion is performed: the RF signal is amplified and then split by bandpass filters, so that — within the limits of the detection bandwidth — the choice of observation frequency is not constrained by the LO frequency or by a filter placed ahead of down-conversion, unlike in the heterodyne schemes. In each panel, red denotes Ch1 and blue denotes Ch2.

Here the ratio of the system noise temperatures of DD and DSB detection is defined as

$$\beta = \frac{T_{\mathrm{sys,DD}}}{T_{\mathrm{sys,DSB}}} \tag{22}$$

Writing the bandwidth of each radio-frequency channel in DD detection as B and the total radio-frequency bandwidth contributing to one IF channel in DSB detection as $2B$, the radiometer equation gives the relation between the observation error variances as

$$\sigma^2_{\mathrm{DSB}} = \frac{\sigma^2_{\mathrm{DD}}}{\alpha},\ \alpha = 2\beta^2 \tag{23}$$

https://doi.org/10.5194/egusphere-2026-6542
Preprint. Discussion started: 10 November 2026
© Author(s) 2026. CC BY 4.0 License.

The condition of equal system noise temperature adopted in this study, $\beta = 1$, therefore corresponds to $\alpha = 2$.

2.5 Sideband asymmetry as the criterion for information loss

As shown in Section 2.4 and, for unequal system noise temperatures, in Section 4.2 (Eqs. 18 and 25), the difference between the inverse retrieval error covariance matrices of the DD and DSB schemes is expressed in terms of the sum $S = K_L + K_U$ and the difference $D = K_L - K_U$ of the LSB and USB Jacobians, and DSB detection carries the same information as DD detection only when the two Jacobians coincide ($D = 0$). The vertical profile of D is therefore a direct indicator of which altitudes the information lost by DSB detection corresponds to.

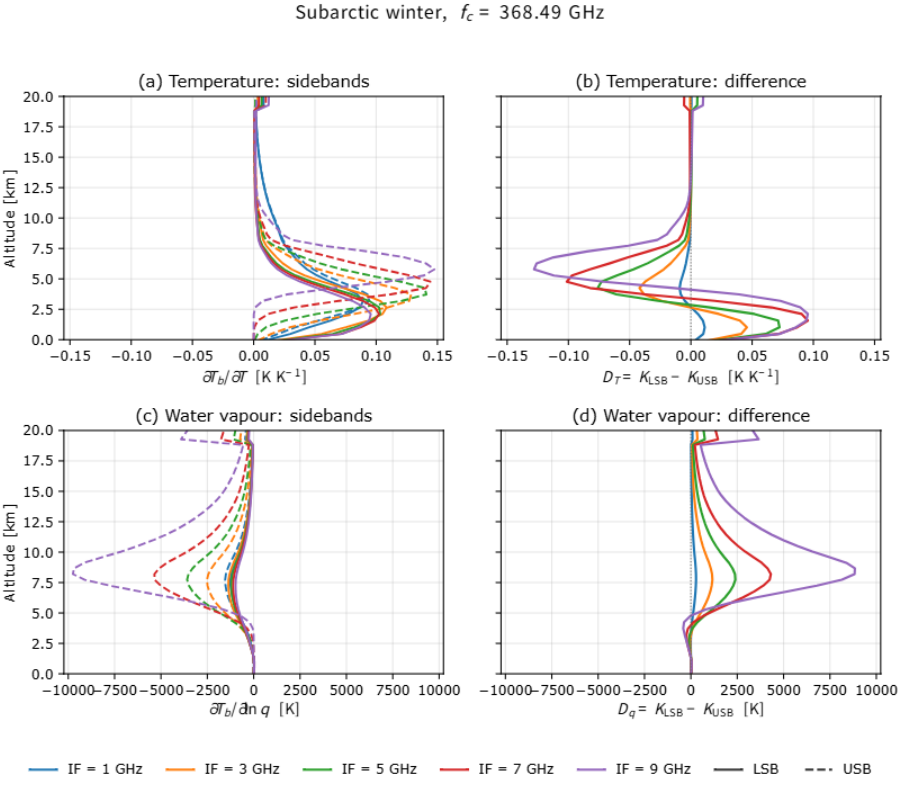
To confirm this concretely, we show the LSB and USB temperature and water-vapour Jacobians and the vertical profile of their difference D for IF = 1, 3, 5, 7 and 9 GHz, taking the subarctic-winter atmosphere as an example, for the 368.49 GHz oxygen band — the only band among the five examined in which a pronounced asymmetry between the LSB and USB Jacobians appears (Figure 7).

The temperature Jacobians (Figure 7a) have their main sensitivity around 2–5 km at every IF and are of broadly similar shape for the LSB and the USB. The difference between the LSB and the USB grows, however, as the IF increases, and at IF = 9 GHz in particular the USB (dashed) shows a systematically larger sensitivity than the LSB (solid) around 5–10 km. As a result, because the USB sensitivity exceeds that of the LSB there, the temperature profile of the difference D (Figure 7b) exhibits a pronounced negative minimum around 5–7.5 km whose magnitude grows with increasing IF.

The same tendency is seen in the water-vapour Jacobians (Figure 7c), but the altitude at which the asymmetry appears is higher than for temperature. At IF = 9 GHz the USB shows a larger sensitivity than the LSB, centred around 7.5–10 km, so the difference D (Figure 7d) has a large maximum around 7.5–10 km, whose amplitude reaches more than twice that of the other IF channels. Because the water-vapour Jacobians are negative, the larger USB sensitivity makes D positive here, in contrast to the negative D for temperature. The same analysis was carried out for the tropical atmosphere (Figure 8). The basic features are shared with the subarctic-winter atmosphere, but because there is more water vapour the amplitude of the difference D between the LSB and the USB is larger.

It is worth noting that the water-vapour difference D has its maximum around 7.5–15 km, whereas the absolute loss of DOFS shown in Section 4.1 is, for some atmospheres, concentrated between 0 and 5 km. We attribute this to the fact that, while D expresses the potential magnitude of the information loss at an individual channel and altitude, the actual effect on the DOFS is determined jointly with the redistribution of information across several channels and altitudes through the vertical correlation of the prior covariance (Section 2.6) and with the contributions of other lines and channels. In other words, D is a qualitative indicator that identifies where an information loss due to the superposition of the LSB and the USB can occur, and does not quantitatively predict the vertical distribution of that loss. This point is discussed again in Section 4.1.

https://doi.org/10.5194/egusphere-2026-6542
Preprint. Discussion started: 10 November 2026
© Author(s) 2026. CC BY 4.0 License.



445

Figure 7 Lower-sideband (LSB) and upper-sideband (USB) Jacobians and their difference D, for the subarctic-winter atmosphere at a centre frequency of 368.49 GHz. (a) Temperature Jacobians, (b) temperature difference $D_T = K_L - K_U$, (c) water-vapour Jacobians, (d) water-vapour difference $D_q = K_L - K_U$. The blue, orange, green, red, and purple lines correspond to IF = 1, 3, 5, 7, and 9 GHz, respectively; solid 450 **lines show the LSB and dashed lines show the USB.**

https://doi.org/10.5194/egusphere-2026-6542
Preprint. Discussion started: 10 November 2026
© Author(s) 2026. CC BY 4.0 License.

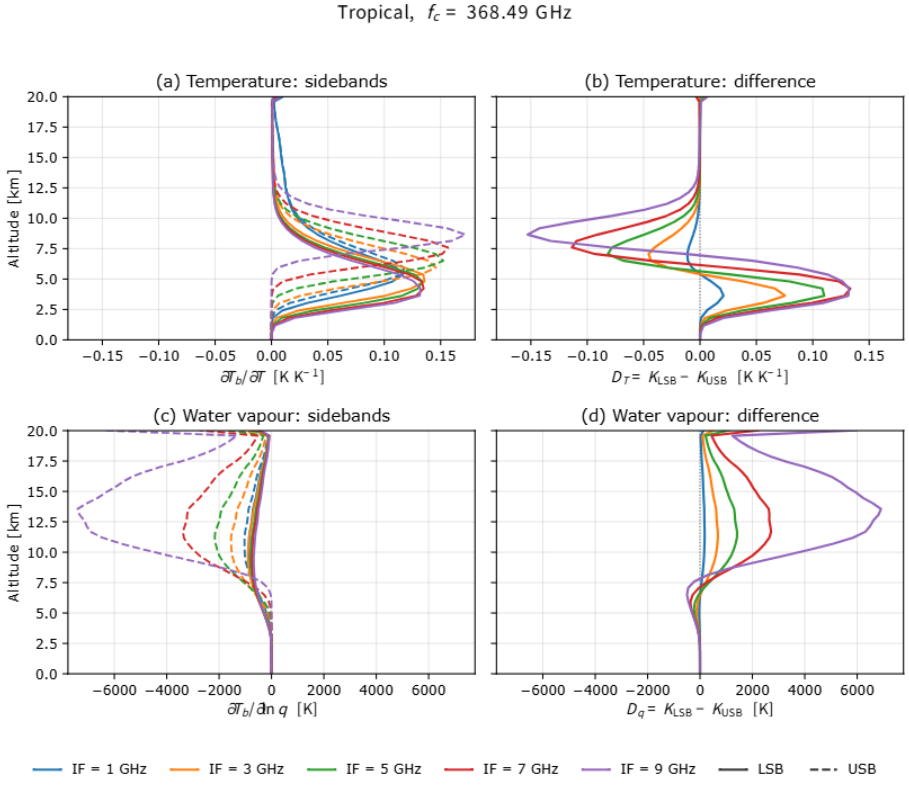


Figure 8 As Figure 7, but for the tropical atmosphere.

2.6 Numerical experiment configuration

We compared the DOFS and the retrieval error of the DD and DSB schemes for the oxygen lines at 118.75 and 368.49 GHz and the water-vapour lines at 183.31, 325.15 and 380.20 GHz. The centre frequency of each line was denoted f_c, and the frequency offset from the line centre, f_{IF}, was set from 1 to 10 GHz in steps of 1 GHz. This IF range was chosen on the basis of the configuration of existing submillimetre sounders. ICI on MetOp-SG is a double-sideband receiver with channels at IF offsets of ±1.5, ±3.5 and ±9.5 GHz in the 325.15 GHz band and ±1.4, ±3.0 and ±7.2 GHz in the 448 GHz band (Eriksson et al., 2020); configurations with an IF of up to about 10 GHz are therefore already in operational use.

The configuration of the IF channels is as given in Section 2.4. For each absorption line we carried out, in addition to an analysis using each IF channel alone, a cumulative analysis in which channels from IF = 1 GHz up to each IF frequency were added successively, and a full-band analysis using all channels from 1 to 10 GHz. The comparison of DD and DSB detection used the difference and the ratio of the DOFS,

https://doi.org/10.5194/egusphere-2026-6542
Preprint. Discussion started: 10 November 2026
© Author(s) 2026. CC BY 4.0 License.



together with the ratio of the retrieval error to the prior error standard deviation at each altitude for temperature, water-vapour VMR and relative humidity.

The observation was assumed to be a satellite nadir observation from an altitude of 200 km (for nadir viewing of a plane-parallel clear-sky atmosphere, the sensor altitude above the top of the model atmosphere does not affect the results), and the line-of-sight angle in ARTS was set to 180 degrees. The atmosphere was taken to be clear-sky and the surface was treated as a blackbody with an emissivity of unity. Pressure, ozone and the other atmospheric constituents were fixed at the values given in each FASCODE standard profile. The main analysis used the tropical and subarctic-winter atmospheres, which have contrasting characteristics in temperature and water-vapour amount.

The vertical grid used for the radiative transfer and Jacobian calculations consisted of 52 levels from about 1023 hPa near the surface to 0.1 Pa at the top of the calculation (Table 1). The atmospheric profiles shown in Figure 1 are also given on this vertical grid. The vertical distributions of the DOFS and of the retrieval error were evaluated mainly from the surface to 20 km altitude, the range targeted by atmospheric sounding. This is because the Jacobian sensitivity of all five bands considered is confined to the troposphere and lower stratosphere (Figure 9b, e), above which the retrieval error is almost equal to the prior error and the contribution to the DOFS is negligible.

The standard deviations of the prior error of temperature and of water-vapour VMR were set to 5 K and to 50 % of the water-vapour VMR at each altitude, respectively. A vertical correlation was imposed within each block of the prior error covariance matrix, the element corresponding to altitudes z_i and z_j being $S_{ij} = \sigma_i \sigma_j \exp\left(-\frac{|z_i - z_j|}{L}\right)$. The correlation length L was set to 2 km for temperature and 1 km for water vapour. The same prior state and the same prior and observation error conditions were used for the comparison of the DD and DSB schemes, so that the difference between them arises only from the detection scheme and not from any difference in the analysis conditions.

An NEDT of 1.0 K was assigned to each observation channel of the DD scheme. For the DSB scheme, taking into account that both the LSB and the USB contribute to the receiving band of a single IF channel, the NEDT was set to

$$\frac{1}{\sqrt{2}}\ \mathrm{K} \simeq 0.71\ \mathrm{K}. \tag{24}$$

The observation errors were taken to be uncorrelated between channels, and the observation error covariance matrix S_ε was constructed as a diagonal matrix whose diagonal elements are the squares of the NEDT of each channel.

In order to evaluate how the information loss due to DSB detection depends on the vertical distribution of water vapour, we further carried out sensitivity experiments in which the RH was altered layer by layer. The troposphere was divided into an upper, a middle and a lower layer, and the conditions in which the RH of each layer was set to 100 % were defined as $\mathrm{RH_H}$, $\mathrm{RH_M}$ and $\mathrm{RH_L}$, respectively. The layer boundaries were set separately for each atmosphere to reflect the difference in tropopause height: 10–15, 5–10 and 0–5 km for the upper, middle and lower layers of the tropical atmosphere, and 5–7.5, 2.5–5 and 0–2.5 km for the subarctic-winter atmosphere. The condition in which all three layers were set to 100 %

https://doi.org/10.5194/egusphere-2026-6542
Preprint. Discussion started: 10 November 2026
© Author(s) 2026. CC BY 4.0 License.

was defined as RH_{HML}, and that in which only the upper and lower layers were set to 100 % as RH_{HL}. In each sensitivity experiment the temperature and pressure profiles were fixed at the values of the reference atmosphere and the water-vapour VMR corresponding to the prescribed RH was recomputed. These saturated layers are an idealised modification of the vertical water-vapour distribution and do not represent cloud: the calculations remain clear-sky, with no condensate and no scattering. The saturation vapour pressure was computed with the formula over water or over ice according to the temperature at each altitude. These five conditions were applied to the tropical and subarctic-winter atmospheres, and the DOFS and the retrieval error of the DD and DSB schemes in the 368.49 GHz band were compared under the same observing and prior error conditions as for the reference atmosphere.

Table 1. Configuration of the radiative transfer calculations and the retrieval error analysis.

Parameter	Specification	Reference
Radiative transfer model	ARTS version 2.6	Buehler et al. (2025)
Spectroscopic line data	H_2O and O_3 lines from the ARTS catalogue (based on HITRAN), line cutoff at 750 GHz	Gordon et al. (2022)
H_2O continuum	MT CKD 4.0 (self and foreign)	Mlawer et al. (2012)
O_2 absorption	PWR2022 model	Rosenkranz (2022); Makarov et al. (2020)
N_2 continuum	PWR2021 self-continuum (including O_2–N_2 and O_2–O_2 collision-induced absorption)	Rosenkranz (2022)
Atmospheric profiles	FASCODE standard atmospheres (tropical and subarctic winter in the main analysis)	Smith et al. (1978)
Observation geometry	Nadir-viewing from 200 km altitude; one-dimensional clear-sky atmosphere	–
Surface	Blackbody (emissivity of 1) with known surface temperature	–
Band centre frequencies	118.75, 183.31, 325.15, 368.49, and 380.20 GHz	–
IF offsets	1–10 GHz in steps of 1 GHz	–
Channel bandwidth	0.5 GHz with rectangular response	–
Detection schemes	DD: upper and lower sidebands as independent channels; DSB: ideal mixer with equal sideband gains	–
NEDT	1.0 K (DD); $\frac{1.0}{\sqrt{2}} \approx 0.71$ K (DSB); uncorrelated between channels	–
Vertical grid	52 pressure levels from the surface to 0.1 Pa (41 levels below 20 km at ≈0.5 km spacing)	–
A priori uncertainty	5 K for temperature; 50 % of the background VMR for water vapour; exponential vertical correlation (L_T = 2 km, L_q = 1 km)	–
Retrieval error analysis	Linearised MAP estimation; DOFS	Rodgers (2000)
Saturation vapour pressure	Tetens-type formulas over water and ice	Tetens (1930); Murray (1967)

https://doi.org/10.5194/egusphere-2026-6542
Preprint. Discussion started: 10 November 2026
© Author(s) 2026. CC BY 4.0 License.

3 Results

3.1 Survey of sideband asymmetry across the 100–400 GHz sounding bands

To assess the symmetry of the temperature and water-vapour Jacobians in the absorption bands of the 100–400 GHz range, we determined the frequency dependence of the maximum of the absolute Jacobian, the altitude of that maximum and the full width at half maximum (FWHM) (Figure 9).

In the water-vapour bands at 183.31, 325.15 and 380.20 GHz the shapes of the temperature and water-vapour Jacobians were broadly symmetric about the line centre. The altitude of the water-vapour Jacobian maximum rose towards the line centre and the FWHM became smaller there, showing that the altitude of the water-vapour sensitivity varies with the frequency offset from the line centre. Temperature sensitivity arises at a water-vapour line because the radiation from the atmosphere also depends on temperature.

At the oxygen lines at 118.75 and 368.49 GHz the maximum of the temperature Jacobian and the altitude of that maximum both increased near the line centre. At 118.75 GHz the Jacobian was broadly symmetric between the low- and high-frequency sides of the line centre. At 368.49 GHz, by contrast, the 380.20 GHz water-vapour line lies about 12 GHz above the line centre, so the influence of water-vapour absorption increases on the high-frequency side and a pronounced asymmetry appears in both the temperature and the water-vapour Jacobians. This asymmetry tended to be larger in moister atmospheres.

https://doi.org/10.5194/egusphere-2026-6542
Preprint. Discussion started: 10 November 2026
© Author(s) 2026. CC BY 4.0 License.

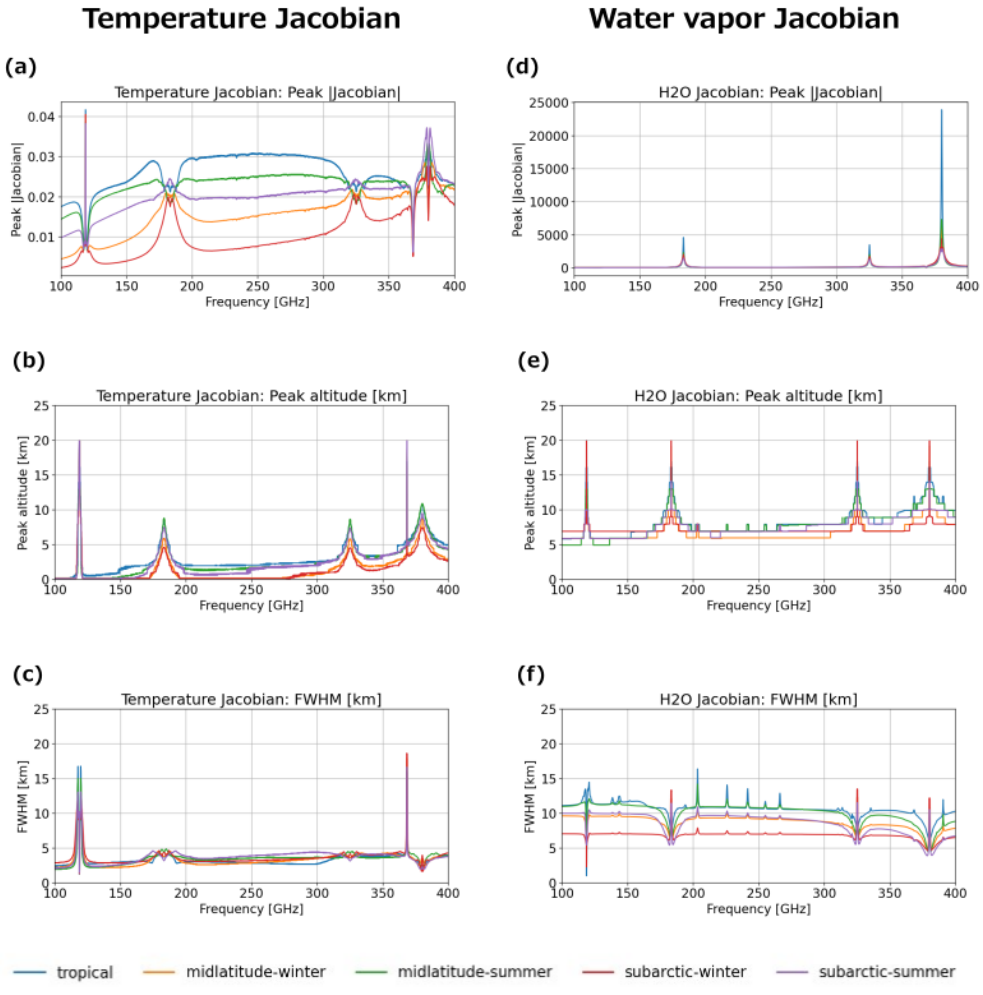


Figure 9 Frequency dependence of characteristic quantities of the temperature Jacobian (a)–(c) and the water-vapour Jacobian (d)–(f), for each atmospheric profile. (a), (d) show the peak absolute value of the Jacobian; (b), (e) show the altitude at which this peak occurs; (c), (f) show the full width at half maximum (FWHM) in the vertical direction. The blue, orange, green, red, and purple lines correspond to the tropical, midlatitude-winter, midlatitude-summer, subarctic-winter, and subarctic-summer atmospheric profiles, respectively.

3.2 Verification: degrees of freedom and the DSB/DD ratio follow the criterion

The DOFS obtained when each IF channel is used on its own was compared with the cumulative DOFS obtained when the channels are added successively from IF = 1 GHz up to each IF channel. At 118.75, 183.31, 325.15 and 380.20 GHz, where the Jacobians are broadly symmetric, the cumulative DOFS of the DSB and DD schemes were almost identical, and the information loss caused by the superposition of the LSB and the USB was small. At 368.49 GHz, by contrast, the cumulative DOFS of

https://doi.org/10.5194/egusphere-2026-6542
Preprint. Discussion started: 10 November 2026
© Author(s) 2026. CC BY 4.0 License.

the DD scheme exceeded that of the DSB scheme as the IF frequency increased, and the difference widened for both temperature and water vapour. This is consistent with the theoretical relation given in Section 2.5 and shows that the asymmetry between the LSB and USB Jacobians causes an information loss in the DSB scheme (Figure 10).

For the DOFS of each IF channel taken alone, the ratio of the DOFS of the DSB scheme to that of the DD scheme was compared. At 118.75, 183.31, 325.15 and 380.20 GHz this ratio was approximately unity, independently of the atmospheric profile and of the IF frequency. At 368.49 GHz, on the other hand, the ratio decreased as the IF frequency increased and reached about 0.50–0.55 at IF = 10 GHz. That is, at 368.49 GHz with IF = 10 GHz the single-channel DOFS retained by the DSB scheme is only about 50–55 % of that of the DD scheme, so that about 45–50 % of the DD degrees of freedom were not retained because of the superposition of the LSB and the USB (Figure 11).

At 368.49 GHz the absolute difference between the DOFS of the DD and DSB schemes was larger for the tropical atmosphere, whereas the ratio of the DOFS of the two schemes was almost the same as for the subarctic-winter atmosphere. This indicates that in the tropical atmosphere the difference between the LSB and USB Jacobians increases while the total amount of information available from the observation increases as well, so that the absolute amount of information lost becomes larger although its fractional share does not change greatly (Figure 10, Figure 11).

These results show that, among the five bands examined, an appreciable information loss arises only in the 368.49 GHz band, because of the 380.20 GHz water-vapour absorption line located about 12 GHz above it (Section 3.1). Of the two RF bands placed symmetrically about the local-oscillator frequency, only the USB approaches this water-vapour line, so that the shape of the Jacobian and the altitude of peak sensitivity differ between the LSB and the USB, and in the DSB scheme the information contained in their difference is lost through superposition.

https://doi.org/10.5194/egusphere-2026-6542
Preprint. Discussion started: 10 November 2026
© Author(s) 2026. CC BY 4.0 License.

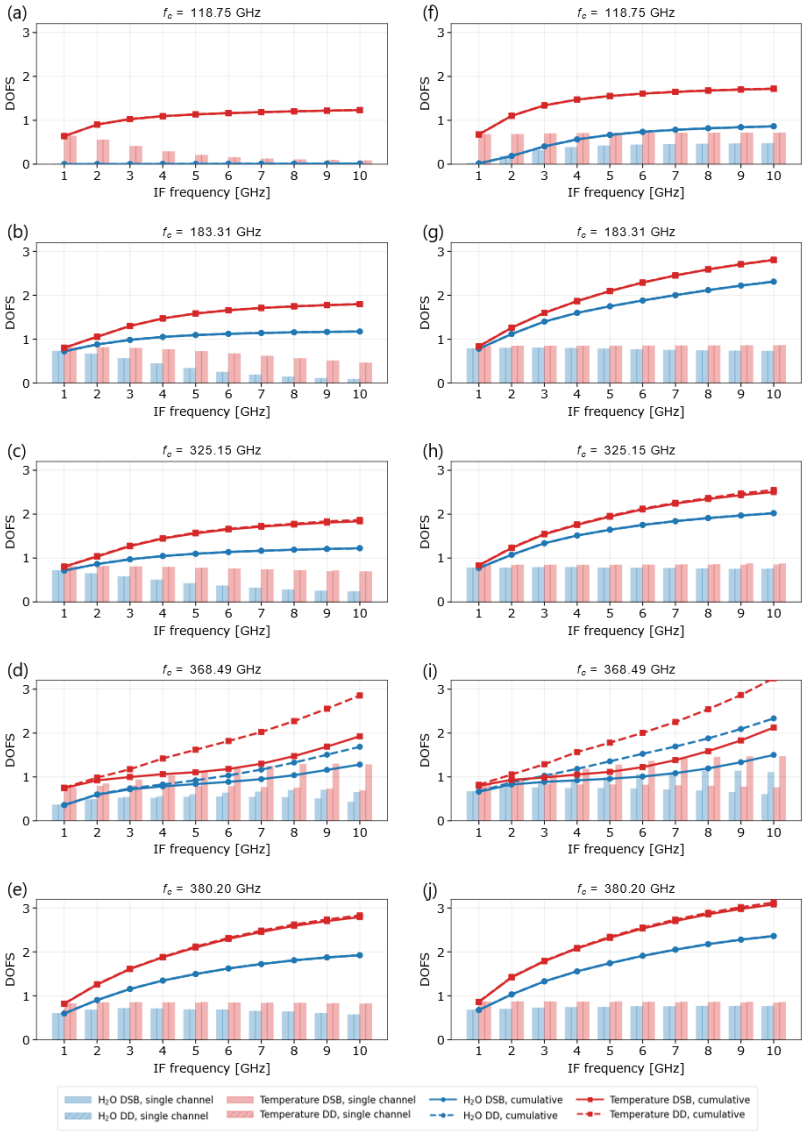


Figure 10 Degrees of freedom for signal (DOFS) for water vapour and temperature. The left column shows results for the subarctic-winter atmosphere, with panels (a)-(e) corresponding, from top to bottom, to the 118.75, 183.31, 325.15, 368.49, and 380.20 GHz observation bands. The right column shows results for the tropical atmosphere, with panels (f)-(j) corresponding to the same bands as the left column, respectively. Blue indicates water vapour and red indicates temperature. The bars show the DOFS for each intermediate-frequency (IF) channel used individually, with unhatched bars showing double-sideband detection (DSB) and hatched bars showing direct detection (DD). The lines show the cumulative DOFS obtained by successively adding channels from IF = 1 GHz up to each IF channel, with solid lines showing

https://doi.org/10.5194/egusphere-2026-6542
Preprint. Discussion started: 10 November 2026
© Author(s) 2026. CC BY 4.0 License.

DSB and dashed lines showing DD. Circles and squares show the cumulative DOFS for water vapour and temperature, respectively.

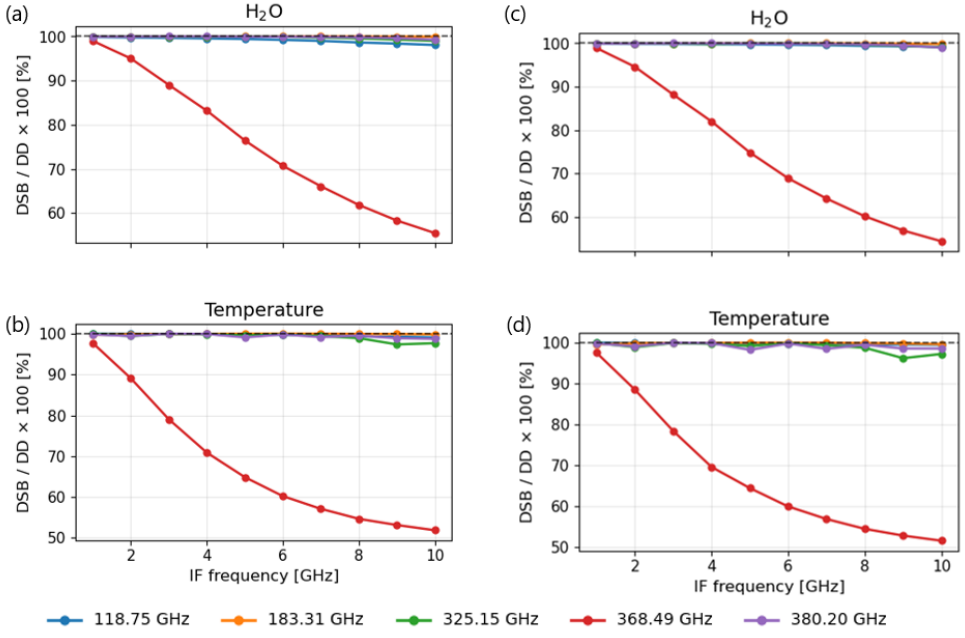


Figure 11 Ratio of the degrees of freedom for signal (DOFS) between DSB and DD detection, expressed as a percentage (DSB/DD × 100), as a function of IF frequency, for water vapour and temperature. The left column shows results for the subarctic-winter atmosphere, with (a) water vapour and (b) temperature; the right column shows results for the tropical atmosphere, with (c) water vapour and (d) temperature. The blue, orange, green, red, and purple lines show this percentage as a function of IF frequency for the 118.75, 183.31, 325.15, 368.49, and 380.20 GHz observation bands, respectively.

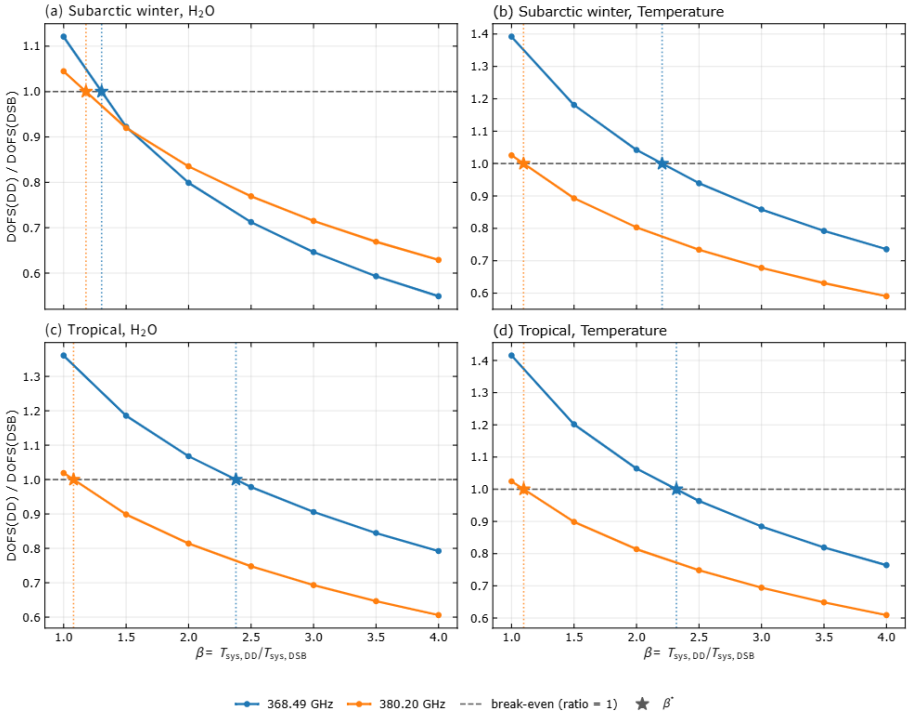
3.3 Sensitivity to the receiver noise ratio and the break-even value

The comparison has so far been restricted to the condition in which the system noise temperatures of the DD and DSB schemes are equal ($\beta = 1$). In an actual receiver design, however, the DD scheme requires two independently filtered RF channels, which may increase the number of filters and detectors relative to a single DSB IF channel, and an equivalent system noise temperature cannot necessarily be achieved. We therefore varied $\beta = \frac{T_{\mathrm{sys,DD}}}{T_{\mathrm{sys,DSB}}}$ from 1 to 4 and determined the break-even noise temperature ratio β^* at which the DOFS of the DD scheme falls below that of the DSB scheme, for 368.49 GHz and, as a reference, for 380.20 GHz, a band whose Jacobians are nearly symmetric (Figure 12).

https://doi.org/10.5194/egusphere-2026-6542
Preprint. Discussion started: 10 November 2026
© Author(s) 2026. CC BY 4.0 License.

At 380.20 GHz, β^* remained close to 1.0 for both temperature and water vapour in both atmospheres, so that the comparative advantage in DOFS reverses in favour of the DSB scheme as soon as the system noise temperature of the DD scheme slightly exceeds that of the DSB scheme. This is because the LSB and USB Jacobians are almost symmetric in this band ($D \approx 0$), so that the advantage of the DD scheme in information content is intrinsically small. At 368.49 GHz, by contrast, β^* was about 1.3 for water vapour in the subarctic-winter atmosphere and about 2.2–2.4 for the other conditions, distinctly larger than at 380.20 GHz. In other words, in the 368.49 GHz band the DD scheme still yields a larger DOFS even when its system noise temperature is appreciably degraded relative to that of the DSB scheme. This result quantifies, under the adopted prior, channel and noise assumptions, the margin in noise performance within which the information loss of the DSB scheme can be avoided in a real receiver. The altitude layers in which the loss is concentrated are discussed in Section 4.1.

It should be noted, however, that β^* varies with the atmospheric condition and with the retrieved quantity (temperature or water vapour), and that, because the present evaluation is based on the DOFS integrated over all layers, the difference between the tropical and subarctic-winter atmospheres seen in the loss restricted to 0–5 km (Section 4.1) may not be fully reflected in this evaluation of β^*. In an actual instrument design it is therefore desirable to evaluate β^* individually for the atmospheric conditions and altitude layers of interest.



https://doi.org/10.5194/egusphere-2026-6542
Preprint. Discussion started: 10 November 2026
© Author(s) 2026. CC BY 4.0 License.

Figure 12 Ratio of the degrees of freedom for signal between direct detection and double-sideband detection, DOFS(DD)/DOFS(DSB), as a function of the receiver noise-temperature ratio $\beta = \frac{T_{sys,DD}}{T_{sys,DSB}}$, for the 368.49 and 380.20 GHz bands. (a) Water vapour and (b) temperature in the subarctic-winter atmosphere; (c) water vapour and (d) temperature in the tropical atmosphere. The blue and orange lines show 368.49 and 380.20 GHz, respectively; the horizontal dashed line marks the break-even ratio of 1, and the stars mark β^*, the value of β at which DOFS(DD) = DOFS(DSB).

3.4 Absolute retrieval error in temperature, water vapour and relative humidity

Section 3.2 showed that in the 368.49 GHz band the DOFS of direct detection (DD) exceeds that of double-sideband detection (DSB) for both water vapour and temperature. This section evaluates the effect of this difference in information content on the retrieval accuracy of temperature, water-vapour volume mixing ratio (VMR) and relative humidity (RH). The prior error, the retrieval error of the DSB scheme and the retrieval error of the DD scheme are shown for each quantity for the subarctic-winter and tropical atmospheres (Figure 13, Figure 14), together with the retrieval error ratio, defined as the retrieval error divided by the prior error. A retrieval error ratio smaller than unity means that the prior error has been reduced by the observation, and the smaller the value the greater the improvement in retrieval accuracy brought by the observation.

In the subarctic-winter atmosphere the retrieval error of temperature is smaller than the prior error from the surface up to about 13 km, so that a reduction of the error by the observation is seen for both the DSB and the DD scheme (Figure 13a, b). The minimum of the retrieval error ratio is about 0.61 at about 3 km for DSB and about 0.54 at about 1.5 km for DD. The retrieval error of DD is smaller than that of DSB at all altitudes, and the difference between the retrieval error ratios of the two schemes is largest in the lower layers, reaching about 0.28 at about 1 km. Above about 13 km the retrieval error ratio of both schemes exceeds 0.95, so that the improvement in temperature retrieval accuracy brought by the 368.49 GHz band becomes small.

For the water-vapour VMR as well, the main error reduction appears between about 2 and 10 km (Figure 13c, d). The absolute value of the retrieval error varies by several orders of magnitude following the vertical variation of the water-vapour VMR, but in terms of the retrieval error ratio the minimum is about 0.90 at about 7 km for DSB and about 0.89 at the same altitude for DD, so that DD gives a slightly larger error reduction. Above about 10 km, on the other hand, the retrieval errors of both DSB and DD are almost equal to the prior error, and the observational information for this altitude range is small.

The retrieval error of RH also improves mainly below about 12 km, as for temperature and water-vapour VMR (Figure 13e, f). The minimum of the retrieval error ratio is about 0.63 at about 7 km for DSB and about 0.60 at the same altitude for DD. The retrieval error of DD is smaller than that of DSB at all altitudes, and the difference between the retrieval error ratios of the two schemes is largest at about 1 km, where it reaches about 0.10. In the subarctic-winter atmosphere, therefore, observing the LSB and the

https://doi.org/10.5194/egusphere-2026-6542
Preprint. Discussion started: 10 November 2026
© Author(s) 2026. CC BY 4.0 License.

USB of the 368.49 GHz band independently retains the information that is lost in DSB detection and improves the retrieval accuracy of RH.

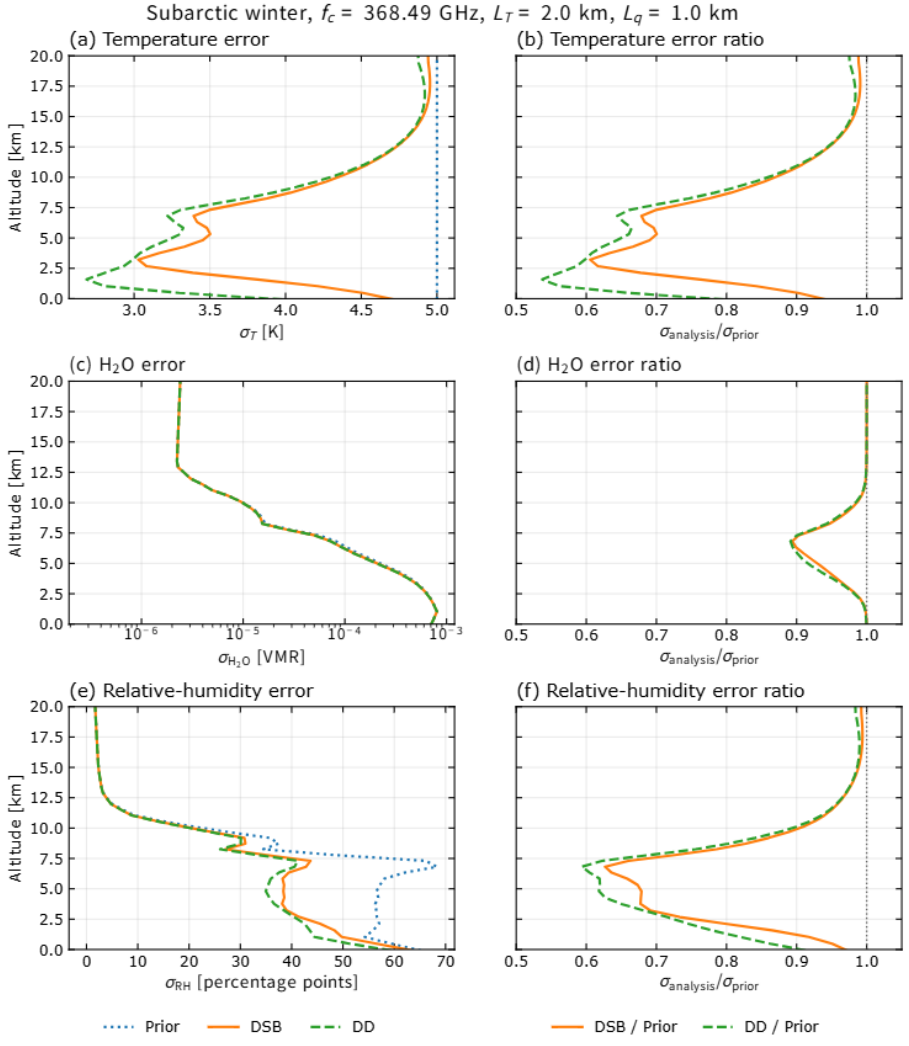
In the tropical atmosphere as well, the retrieval errors of temperature, water-vapour VMR and RH are reduced mainly between about 2 and 13 km (Figure 14). For temperature, the retrieval error of DD is smaller than that of DSB between about 2 and 13 km (Figure 14a, b). The minimum of the retrieval error ratio is about 0.68 at about 5.5 km for DSB, whereas for DD it falls to about 0.64 at about 9 km. The difference between the retrieval error ratios of the two schemes is largest at about 3 km, where it reaches about 0.22, so that an improvement in temperature retrieval accuracy by DD is found in the tropical atmosphere as well.

Because the tropical atmosphere contains more water vapour than the subarctic-winter atmosphere, the absolute values of the prior and retrieval errors of the water-vapour VMR are larger (Figure 14c). When evaluated as a ratio to the prior error, however, the retrieval error ratio of DD is found to be smaller than that of DSB between about 4 and 10 km (Figure 14d). The minimum of the retrieval error ratio is about 0.91 for DSB and about 0.90 for DD, and the difference between the retrieval error ratios of the two schemes is largest at about 4.5 km, where it is about 0.05. Hence DD retains more water-vapour information than DSB also under atmospheric conditions with a different absolute water-vapour VMR.

For RH, a reduction of the retrieval error by the observation is found between about 2 and 13 km, and the retrieval error of DD is smaller than that of DSB (Figure 14e, f). The minimum of the retrieval error ratio is about 0.64 at about 6 km for DSB and about 0.61 at about 8 km for DD, and the difference between the retrieval error ratios of the two schemes is largest at about 3.5 km, where it reaches about 0.19. Above about 13 km, on the other hand, the retrieval error ratio is almost unity for temperature, water-vapour VMR and RH alike, and no clear error reduction is obtained with either scheme.

These results show that observations in the 368.49 GHz band improve the retrieval accuracy of temperature, water-vapour VMR and RH mainly below about 13 km in both the subarctic-winter and the tropical atmosphere. Moreover, under matched system noise temperature, integration time and total RF bandwidth, the retrieval error of DD was consistently smaller than that of DSB. This is because the 380.20 GHz water-vapour absorption line lying close above the 368.49 GHz oxygen absorption line makes the LSB and USB Jacobians asymmetric: in the DSB scheme the information contained in their difference is lost through superposition, whereas in the DD scheme it is retained as independent observational information. It is thus confirmed that the information loss of the DSB scheme, shown in terms of the DOFS in Section 3.2, also appears as an increase in the retrieval error of temperature, water-vapour VMR and RH. If this asymmetry originates in the presence of the water-vapour absorption line, the magnitude of the information loss due to DSB detection is expected to vary with the amount of water vapour and with its vertical distribution.

https://doi.org/10.5194/egusphere-2026-6542
Preprint. Discussion started: 10 November 2026
© Author(s) 2026. CC BY 4.0 License.



695 **Figure 13** Evaluation of the reduction in retrieval error relative to the prior error, for temperature, water vapour, and relative humidity, for observations at a centre frequency of 368.49 GHz in the subarctic-winter atmosphere, with L_T = 2.0 km and L_q = 1.0 km. (a), (c), (e) show the absolute error for temperature, water vapour, and relative humidity, respectively; (b), (d), (f) show the corresponding ratio of the retrieval error to the prior
700 error. The blue dotted, orange solid, and green dashed lines show the prior error, the double-sideband (DSB) retrieval error, and the direct-detection (DD) retrieval error, respectively.

https://doi.org/10.5194/egusphere-2026-6542
Preprint. Discussion started: 10 November 2026
© Author(s) 2026. CC BY 4.0 License.

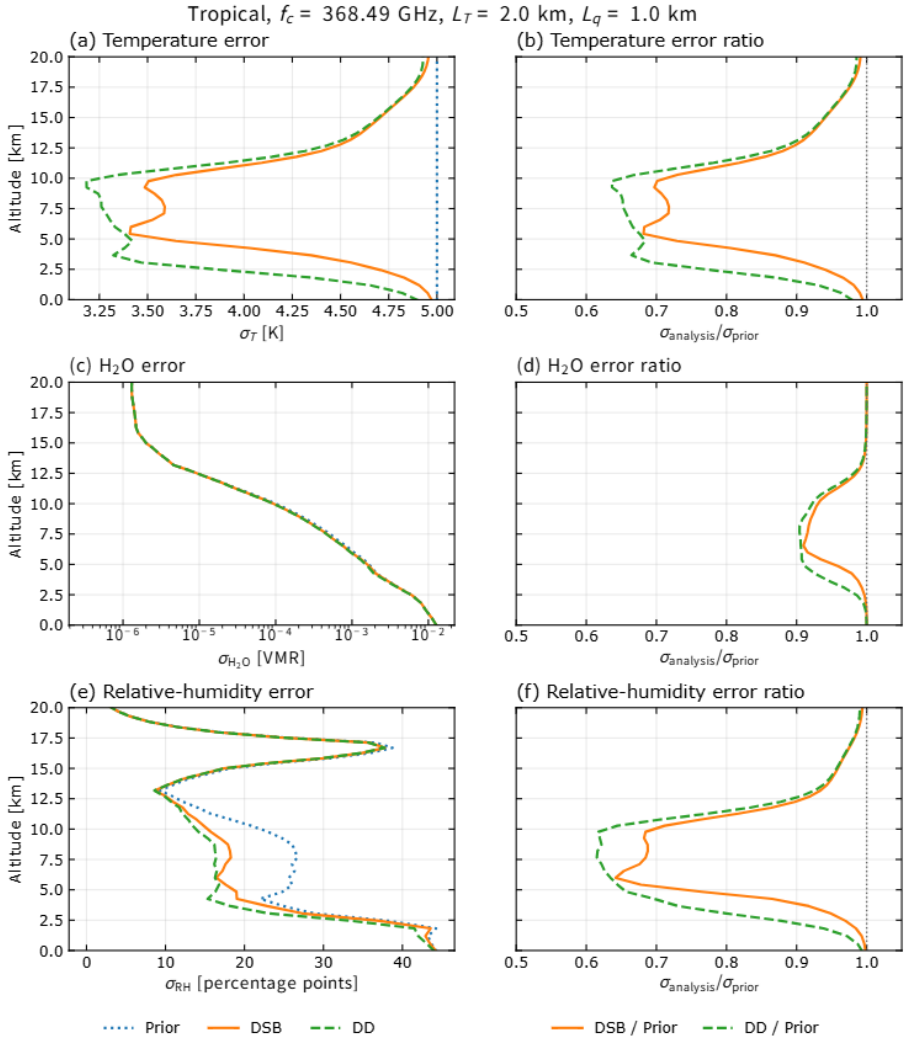


Figure 14 As Figure 13, but for the tropical atmosphere. (a), (c), (e) show the absolute error for temperature, water vapour, and relative humidity, respectively; (b), (d), (f) show the corresponding ratio of the retrieval error to the prior error. The blue dotted, orange solid, and green dashed lines show the prior error, the double-sideband (DSB) retrieval error, and the direct-detection (DD) retrieval error, respectively.

3.5 Effect of RH variation and saturated conditions

Since the information loss of the DSB scheme originates in the difference between the LSB and USB Jacobians, its magnitude is expected to depend not only on the amount of water vapour in the atmosphere but also on its vertical distribution. We therefore compared the RH retrieval errors of the subarctic-winter and tropical atmospheres for the five RH sensitivity experiments defined in Section 2.6 (Figures 15–18).

https://doi.org/10.5194/egusphere-2026-6542
Preprint. Discussion started: 10 November 2026
© Author(s) 2026. CC BY 4.0 License.

In the subarctic-winter atmosphere the retrieval error ratio of DD was smaller than that of DSB at all altitudes under every saturation condition (Figures 15, 16). The minimum of the retrieval error ratio was about 0.65–0.67 for DSB and about 0.62–0.64 for DD, at around 7 km, and the differences between the saturation conditions were small. The difference between DSB and DD was largest at around 1 km, where it was about 0.09 for each of the single-layer saturation cases RH_H, RH_M and RH_L, and about 0.10–0.11 for the multiple-layer saturation cases RH_{HML} and RH_{HL}. In the subarctic-winter atmosphere, therefore, although an advantage of DD due to the increase in RH is found, its magnitude was almost independent of the altitude and the number of the saturated layers.

In the tropical atmosphere the difference between the retrieval error ratios of DSB and DD was about twice as large as in the subarctic-winter atmosphere (Figures 17, 18). For RH_M, in which the middle layer was saturated, the difference reached a maximum of about 0.20 at around 5 km, the minimum of the retrieval error ratio being about 0.66 for DSB and about 0.60 for DD (Figure 17e). For RH_L, in which the lower layer was saturated, the difference reached a maximum of about 0.18 at around 4.5 km, the minimum of the retrieval error ratio being about 0.70 for DSB and about 0.64 for DD (Figure 17f). For RH_H, in which the upper layer was saturated, the difference also reached about 0.17 at around 4 km.

Comparable differences were found under the conditions in which several layers were saturated. For RH_{HML}, in which 0–15 km was saturated continuously, the difference reached a maximum of about 0.21 at around 5 km (Figure 18c). For RH_{HL}, in which the upper and lower layers were saturated but the middle layer was not, the difference reached a maximum of about 0.18 at around 4.5 km, the minimum of the retrieval error ratio being about 0.70 for DSB and about 0.64 for DD (Figure 18d). In the tropical atmosphere, therefore, the difference between the retrieval error ratios lay in the range of about 0.17–0.21 under every condition, irrespective of the altitude and the number of the saturated layers.

These results show that, within the range of the present sensitivity experiments, the magnitude of the information loss of the DSB scheme in the 368.49 GHz band corresponds more clearly to the absolute amount of water vapour, the differences due to the vertical arrangement of the saturated layers being relatively small. In the tropical atmosphere, with its large saturation water-vapour amount, the difference between the retrieval error ratios reached about 0.17–0.21, roughly twice the value of about 0.09–0.11 obtained for the subarctic-winter atmosphere. We attribute this to the fact that, as the amount of water vapour increases, the difference between the LSB and USB Jacobians widens overall, and in the DSB scheme the information contained in that difference is lost through superposition. The differences caused by the altitude at which the saturated layer is placed, and by the number of saturated layers, were small in both atmospheres. It should be noted, however, that the present sensitivity experiments did not vary the vertical distribution alone while keeping the total water-vapour amount constant, so that the effect of the absolute amount and that of the vertical distribution are not strictly separated.

https://doi.org/10.5194/egusphere-2026-6542
Preprint. Discussion started: 10 November 2026
© Author(s) 2026. CC BY 4.0 License.

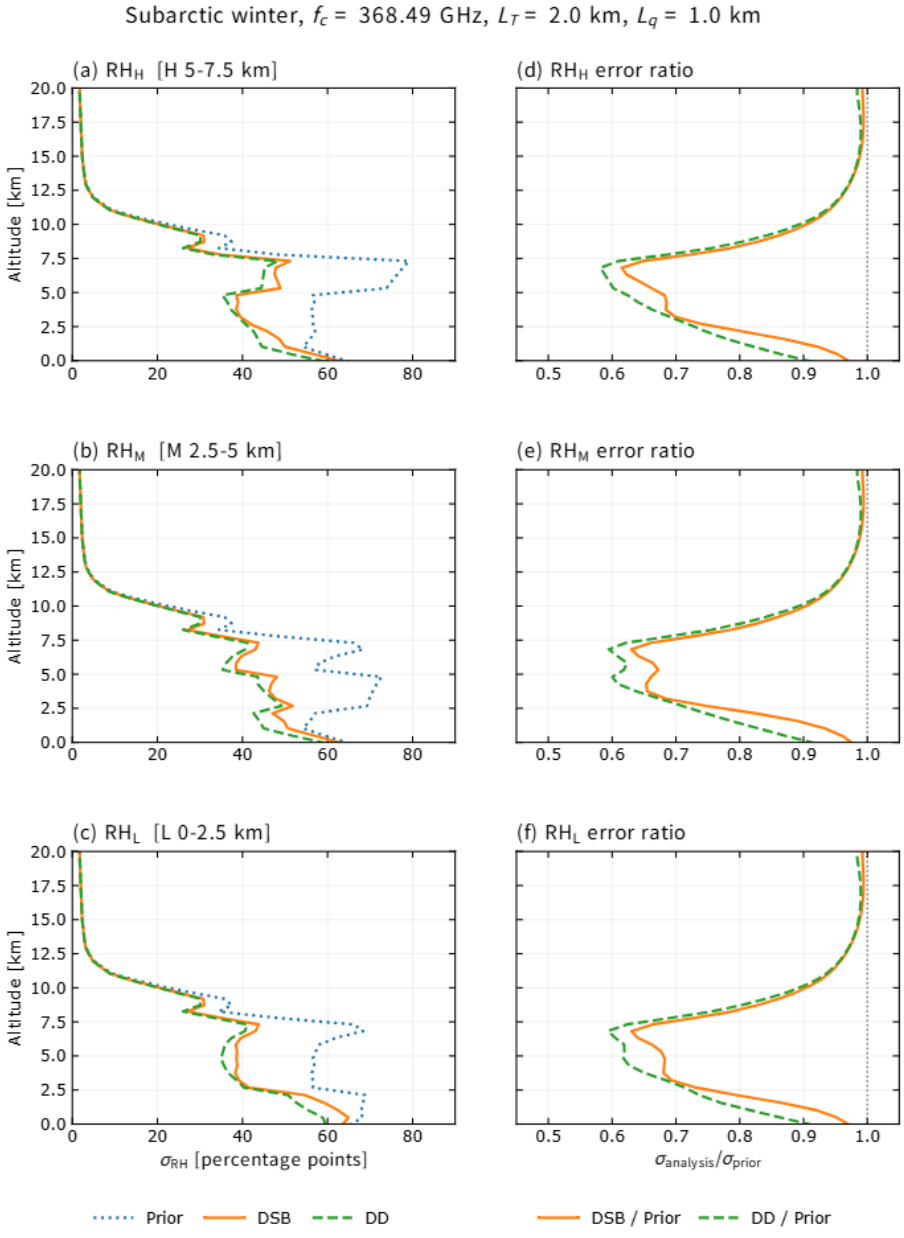


Figure 15 Evaluation of the reduction in retrieval error relative to the prior error for relative humidity, for observations at a centre frequency of 368.49 GHz in the subarctic-winter atmosphere, with L_T = 2.0 km and L_q = 1.0 km. (a)-(c) show the absolute error for RH$_H$ [H: 5-7.5 km], RH$_M$ [M: 2.5-5 km], and RH$_L$ [L: 0-2.5 km], respectively; (d)-(f) show the corresponding ratio of the retrieval error to the prior error. The blue dotted, orange solid,

https://doi.org/10.5194/egusphere-2026-6542
Preprint. Discussion started: 10 November 2026
© Author(s) 2026. CC BY 4.0 License.

and green dashed lines show the prior error, the double-sideband (DSB) retrieval error, and the direct-detection (DD) retrieval error, respectively.

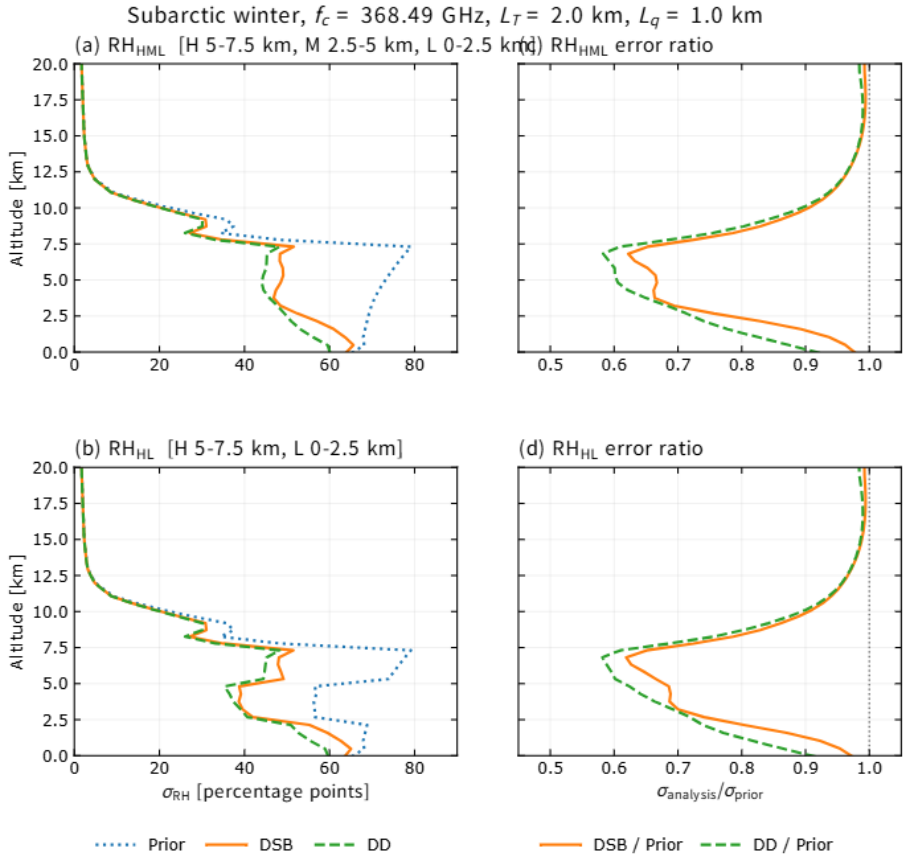


Figure 16 As Figure 15, but showing the combined altitude ranges RH$_{HML}$ [H: 5–7.5 km, M: 2.5–5 km, L: 0–2.5 km] and RH$_{HL}$ [H: 5–7.5 km, L: 0–2.5 km]. (a), (b) show the absolute error for RH$_{HML}$ and RH$_{HL}$, respectively; (c), (d) show the corresponding ratio of the retrieval error to the prior error.

https://doi.org/10.5194/egusphere-2026-6542
Preprint. Discussion started: 10 November 2026
© Author(s) 2026. CC BY 4.0 License.

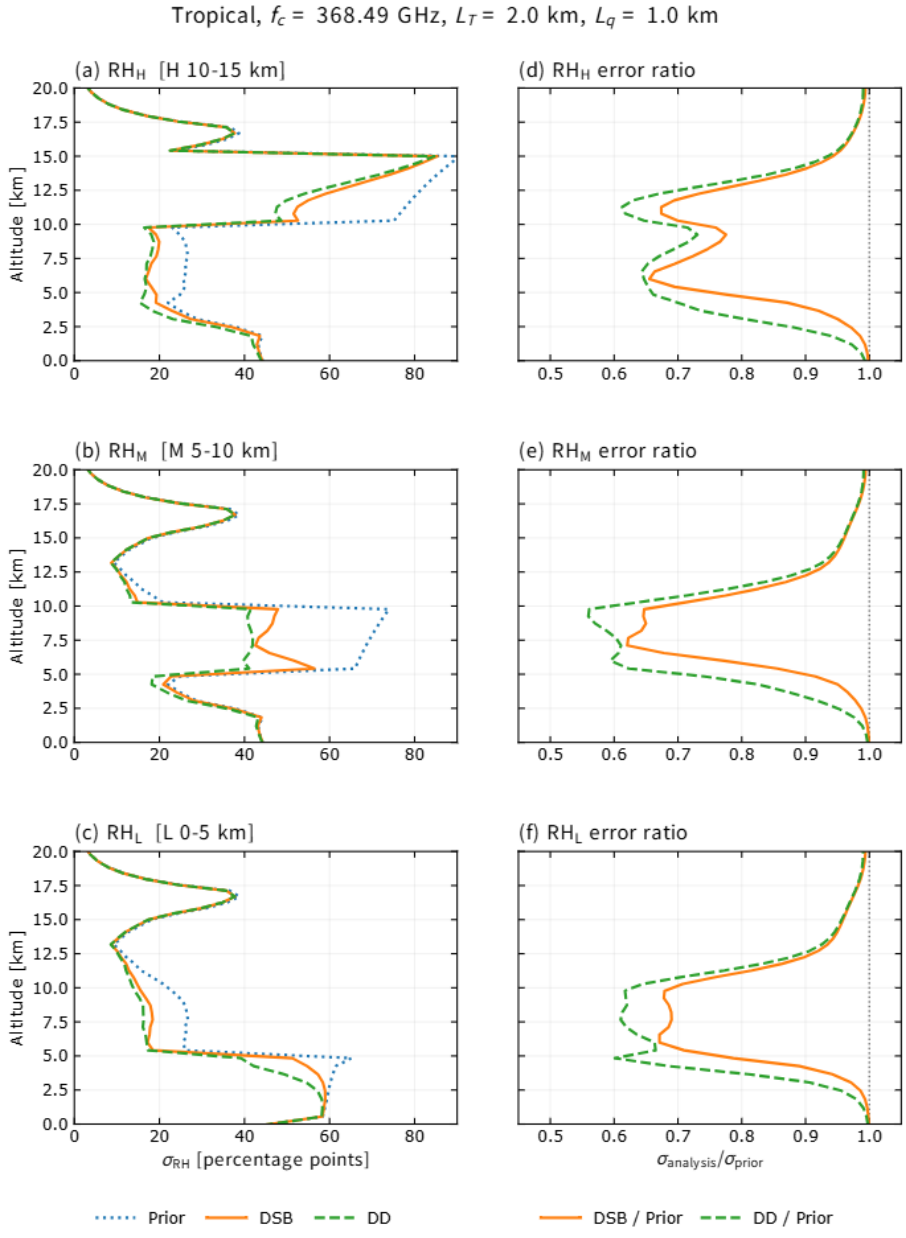


Figure 17 As Figure 15, but for the tropical atmosphere. (a)–(c) show the absolute error for RH$_H$ [H: 10–15 km], RH$_M$ [M: 5–10 km], and RH$_L$ [L: 0–5 km], respectively; (d)–(f) show the corresponding ratio of the retrieval error to the prior error.

765

https://doi.org/10.5194/egusphere-2026-6542
Preprint. Discussion started: 10 November 2026
© Author(s) 2026. CC BY 4.0 License.

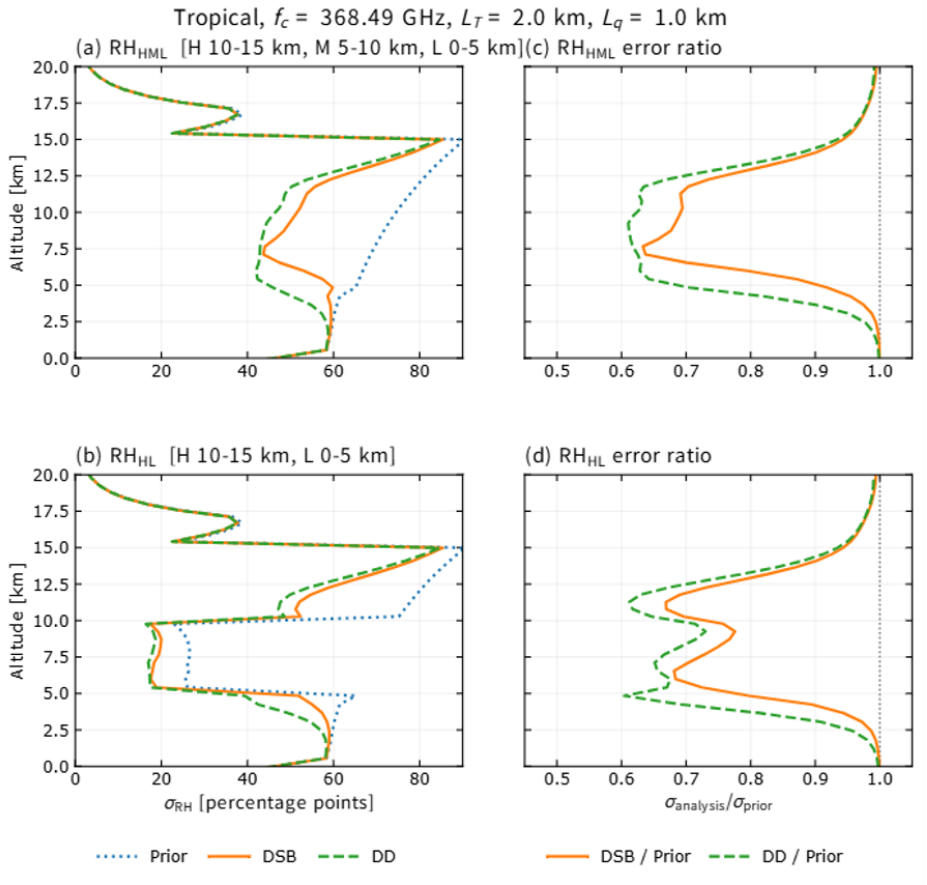


Figure 18 As Figure 16, but for the tropical atmosphere, with RH_{HML} [H: 10–15 km, M: 5–10 km, L: 0–5 km] and RH_{HL} [H: 10–15 km, L: 0–5 km].

770

4 Discussion

4.1 Altitude dependence of DSB information loss

As shown in Section 3, of the five absorption bands examined, the information loss of the DSB scheme appears appreciably only in the 368.49 GHz band. It should be noted that the present study does not
775 address the selection of the observation bands themselves. The 368.49 GHz band is one that next-generation submillimetre sounders already target, and the question here is which detection scheme should be used to observe it. In this section the temperature and water-vapour DOFS of the DD and DSB schemes are compared layer by layer for the 0–5 km and 5–10 km altitude ranges (Table 2). In addition,

https://doi.org/10.5194/egusphere-2026-6542
Preprint. Discussion started: 10 November 2026
© Author(s) 2026. CC BY 4.0 License.

the DOFS retention of the DSB scheme relative to the DD scheme (DSB/DD × 100 [%]) at 368.49 GHz is summarised layer by layer (Table 3). In the four bands at 118.75, 183.31, 325.15 and 380.20 GHz the retention lies between 95 and 100 % for every atmosphere, layer and quantity (except for water vapour at 118.75 GHz over 5–10 km in the tropical atmosphere, a layer whose absolute DOFS is below 0.02 and which therefore carries no significant information), so that the information loss of the DSB scheme is effectively negligible.

At 368.49 GHz, by contrast, the retention over 0–5 km is systematically lower than over 5–10 km. For temperature it is 38.8 % in the tropical atmosphere and 62.8 % in the subarctic-winter atmosphere, whereas over 5–10 km it is 84.4 % and 89.7 %, respectively. Water vapour shows the same tendency: the retention over 0–5 km is only 26.9 % in the tropical atmosphere and 82.1 % in the subarctic-winter atmosphere, while over 5–10 km it recovers to 86.1 % and 92.4 %, respectively. The information loss at 368.49 GHz therefore does not occur uniformly throughout the troposphere but is concentrated between 0 and 5 km.

The magnitude of this loss depends, moreover, strongly on how moist the atmosphere is. In the tropical atmosphere, which contains much water vapour, the water-vapour DOFS over 0–5 km is 0.191 for the DD scheme and 0.051 for the DSB scheme, a retention of about one quarter. In the subarctic-winter atmosphere, which contains little water vapour, the corresponding values in the same layer are 0.180 and 0.148, so that the loss is small both in absolute terms and in terms of retention. This is consistent with the tendency shown in Section 3.2, namely that in the tropical atmosphere both the difference between the LSB and USB Jacobians and the absolute amount of observational information increase, so that the absolute amount of information lost becomes larger; it shows that, at least for water vapour over 0–5 km, this effect also appears clearly in the layer-by-layer breakdown of the DOFS.

Restricted to 0–5 km, the temperature DOFS obtained by observing 368.49 GHz with the DD scheme exceeds that obtained by observing 380.20 GHz with the DSB scheme (0.830 against 0.343 in the tropics, 1.635 against 1.315 in subarctic winter). Over 5–10 km, on the other hand, the relation is reversed (1.475 against 1.616 in the tropics, 0.954 against 1.158 in subarctic winter). This reversal arises because the 380.20 GHz water-vapour line absorbs more strongly than the 368.49 GHz oxygen line and becomes optically thick in the middle troposphere (Figure 3). Indeed, the temperature DOFS of 380.20 GHz over 0–5 km falls from 1.318 in the dry subarctic-winter atmosphere to 0.349 in the moist tropical atmosphere, a reduction to about one quarter (Table 2), because as the amount of water vapour increases the absorption saturates and the effective emission height no longer reaches the lower troposphere. The temperature DOFS of 368.49 GHz in the same layer, by contrast, falls only from 1.635 to 0.830. The two bands are thus complementary in altitude: because 380.20 GHz carries almost no temperature information over 0–5 km in a moist atmosphere, it cannot compensate for the information lost by DSB detection at 368.49 GHz. The information is not entirely lost with the DSB scheme either, since a DOFS of 0.322 for temperature and 0.051 for water vapour remains over 0–5 km in the tropical atmosphere. Observing 368.49 GHz with the DD scheme is nevertheless effective if the information of this layer is to be sufficiently retained.

https://doi.org/10.5194/egusphere-2026-6542
Preprint. Discussion started: 10 November 2026
© Author(s) 2026. CC BY 4.0 License.

Operating the 368.49 GHz band with the DSB scheme therefore incurs its largest penalty in information content for water-vapour sounding over 0–5 km under moist atmospheric conditions. The extent to which this penalty can be offset by the noise performance of the receiver is as shown in Section 3.3.

Table 2. Partial degrees of freedom for signal in the 0–5 km and 5–10 km layers, for temperature and water vapour, obtained with direct detection (DD) and double-sideband detection (DSB) in (a) the tropical and (b) the subarctic-winter atmosphere. Values are from the joint retrieval of temperature and water vapour with a vertically correlated prior (correlation lengths of 2 km for temperature and 1 km for water vapour), a receiver noise ratio of $\beta = 1$, and $\mathrm{NEDT}_{\mathrm{DSB}} = \frac{\mathrm{NEDT}_{\mathrm{DD}}}{\sqrt{2}}$. The largest value in each column is shown in bold. Values below 0.02 are not considered meaningful. Clear-sky conditions are assumed throughout.

(a) Tropical

Centre frequency (GHz)	Species	Temperature				Water vapour			
		0–5 km		5–10 km		0–5 km		5–10 km	
		DD	DSB	DD	DSB	DD	DSB	DD	DSB
118.75	O_2	0.861	0.857	0.419	0.419	0.257	0.252	0.017	0.014
183.31	H_2O	**1.285**	**1.283**	0.931	0.930	**0.336**	**0.335**	0.524	0.523
325.15	H_2O	1.027	1.013	0.975	0.974	0.223	0.220	0.536	0.534
368.49	O_2	0.830	0.322	1.475	1.245	0.191	0.051	0.582	0.501
380.20	H_2O	0.349	0.343	**1.619**	**1.616**	0.069	0.068	**0.602**	**0.593**

(b) Subarctic winter

Centre frequency (GHz)	Species	Temperature				Water vapour			
		0–5 km		5–10 km		0–5 km		5–10 km	
		DD	DSB	DD	DSB	DD	DSB	DD	DSB
118.75	O_2	0.800	0.800	0.565	0.565	0.010	0.010	0.003	0.003
183.31	H_2O	1.331	1.330	0.324	0.324	0.154	0.154	0.291	0.291
325.15	H_2O	1.364	**1.363**	0.308	0.308	0.155	0.155	0.286	0.286
368.49	O_2	**1.635**	1.027	0.954	0.856	0.180	0.148	**0.432**	**0.399**
380.20	H_2O	1.318	1.315	**1.164**	**1.158**	**0.188**	**0.183**	0.405	0.385

Table 3. Fraction of the direct-detection degrees of freedom retained by double-sideband detection (DSB/DD, %) at 368.49 GHz. The corresponding values for the other four bands lie between 95 % and 100 % in every layer and for both variables, with the single exception of water vapour at 118.75 GHz in the tropical atmosphere between 5 and 10 km, where the absolute degrees of freedom are below 0.02.

https://doi.org/10.5194/egusphere-2026-6542
Preprint. Discussion started: 10 November 2026
© Author(s) 2026. CC BY 4.0 License.

Atmosphere	Temperature		Water vapour	
	0–5 km	5–10 km	0–5 km	5–10 km
Tropical	38.8	84.4	26.9	86.1
Subarctic winter	62.8	89.7	82.1	92.4

4.2 Implications for instrument design at 368.49 GHz

Using the system noise temperature ratio β, the difference between the inverse retrieval error covariance matrices of the DD and DSB schemes is expressed as

$$\hat{S}_{\mathrm{DD}}^{-1} - \hat{S}_{\mathrm{DSB}}^{-1} = \frac{1}{4\sigma_{\mathrm{DD}}^2}[(2-\alpha)(K_L+K_U)^{\mathrm{T}}(K_L+K_U) + 2(K_U-K_L)^{\mathrm{T}}(K_U-K_L)] \quad (25)$$

In particular, under the comparison condition adopted in this study, $\alpha = 2$, the first term vanishes and the expression reduces to Eqs. (18)–(21) of Section 2.4.

When the system noise temperature ratio satisfies $\beta \leq 1$, that is, when the system noise temperature of the DD scheme is not larger than that of the DSB scheme, the two terms constituting the above expression are both positive semi-definite, so that the advantage of the DD scheme is likewise guaranteed. When $\beta > 1$, on the other hand, the coefficient of the term corresponding to the sum S of the Jacobians becomes negative, so that the general ordering of the DD and DSB schemes cannot be determined from the theoretical expression alone; the boundary is given by the β^* presented in Section 3.3. In choosing a detection scheme it is therefore necessary to consider not only the frequency placement with respect to the line centre, but also the asymmetry between the LSB and USB Jacobians, including the effects of nearby absorption lines and of the continuum, together with the system noise temperature ratio that can be realised.

4.3 Limitations

This study has several limitations. First, the radiative transfer calculations assume a clear-sky atmosphere and do not take into account scattering and attenuation by cloud and precipitation. In real observations the information loss due to cloud could affect the comparison between DSB and DD detection, so it should be borne in mind that the conclusions presented here are an evaluation under clear-sky conditions.

Second, the observation error is assumed to consist only of thermal noise expressed by the NEDT, and 1/f noise arising from receiver gain fluctuation (the gain-fluctuation term in Eq. 14) is not considered. If the contribution of 1/f noise differs between DD and DSB detection, the comparison presented here could change.

Third, DD detection requires two independently filtered RF channels and may therefore increase the number of filters and detectors relative to a single DSB IF channel; whether the amplifier stages can be

https://doi.org/10.5194/egusphere-2026-6542
Preprint. Discussion started: 10 November 2026
© Author(s) 2026. CC BY 4.0 License.

shared depends on the actual configuration. Moreover, while LNA-based DD receivers have been demonstrated up to the 300 GHz range (Tessmann et al., 2017), their feasibility at 368–380 GHz remains to be demonstrated, and the DD scheme considered here should be regarded as a conceptual architecture. This study is confined to a comparison from the standpoint of information content, in terms of the DOFS and the retrieval error, and does not evaluate instrument design constraints such as cost, power consumption and mass.

Fourth, the prior error covariance matrix is set with the temperature and water-vapour blocks independent (Section 2.3), and the vertical correlation between them is not taken into account. If a physical correlation exists between temperature and water vapour, the absolute values of the DOFS and of the retrieval error could differ from those obtained here. Since the comparison of DD and DSB detection uses the same prior covariance matrix, however, the effect of this simplification on the conclusions regarding the relative merits of the two schemes is expected to be limited.

Fifth, the FASCODE standard atmospheres were used for the atmospheric profiles, so that the day-to-day variability of the real atmosphere is not represented. The variability of the water-vapour amount in particular directly affects the magnitude of the information loss of the DSB scheme (Section 3.5), and the quantitative results presented here should therefore be interpreted as a representative evaluation within the range of the standard atmospheric profiles.

Sixth, the main analysis was carried out with the vertical correlation lengths of the prior covariance fixed at L_T = 2 km and L_q = 1 km. Since the same prior covariance matrix is used for the comparison of the DD and DSB schemes, the choice of the correlation lengths is not expected to alter the conclusions concerning their relative merits, but the absolute values of the DOFS do depend on the correlation lengths. The effect of varying the correlation lengths of temperature and water vapour independently has, however, been examined only to a limited extent. Nor has the dependence of the absolute DOFS on the vertical grid spacing been examined; with the vertically correlated prior used here this dependence is expected to be weak, but the values reported refer to the 52-level grid of Table 1.

Seventh, this study assumed an ideal DSB receiver in which the sideband gains of the LSB and the USB are equal and the frequency response of the channel is rectangular (Section 2.4). The effect on the comparison between the DD and DSB schemes of deviations of the sideband ratio in a real instrument, and of the errors in its calibration, needs to be examined in future work.

Eighth, the comparison between bands is based on the DOFS linearised about the reference atmospheric profiles. The temperature information carried by a water-vapour absorption line is conditioned on the accuracy of the water-vapour retrieval and on the prior information, because the effective emission height depends on the vertical distribution of water vapour. The volume mixing ratio of oxygen, by contrast, is known and almost constant, so that the weighting function of an oxygen absorption line is determined by pressure alone. This difference in robustness does not appear in the DOFS, and the DOFS comparison between bands made here cannot therefore be used directly as a criterion for selecting observation bands. Finally, as shown in Section 2.5, the vertical profile of the difference D between the LSB and USB Jacobians does not directly predict the altitudes at which an

https://doi.org/10.5194/egusphere-2026-6542
Preprint. Discussion started: 10 November 2026
© Author(s) 2026. CC BY 4.0 License.

absolute loss of DOFS occurs. D is a qualitative indicator that identifies where an information loss can occur, and evaluating the vertical distribution of the actual loss requires a direct calculation of the DOFS including the prior covariance, as performed in this study.

5 Conclusions

In this study the loss of observational information caused by double-sideband (DSB) detection in millimetre- and submillimetre-wave radiometers was quantified theoretically and numerically by comparison with direct detection (DD). Under an idealised comparison condition in which the system noise temperature, the integration time and the total RF bandwidth contributing to the detection are matched, the difference between the inverse retrieval error covariance matrices of the DD and DSB schemes was derived, and the DOFS and the retrieval errors were evaluated for five absorption bands at 118.75, 183.31, 325.15, 368.49 and 380.20 GHz by a MAP error analysis using radiative transfer calculations with ARTS and the FASCODE standard atmospheres. The conclusions obtained are as follows.

(1) Under the system noise temperature ratio $\beta = 1$ (the matched condition), the difference between the inverse retrieval error covariance matrices of the DD and DSB schemes is a Gram matrix and hence positive semi-definite, so that the retrieval error variance of the DD scheme is theoretically guaranteed not to exceed that of the DSB scheme. Equality holds only when the LSB and USB Jacobians coincide. This guarantee holds irrespective of the dimension of the state vector.

(2) At 118.75, 183.31, 325.15 and 380.20 GHz the LSB and USB Jacobians are broadly symmetric, and the ratio of the DOFS of the DD and DSB schemes was approximately unity irrespective of the atmospheric profile and of the IF frequency. In these bands the information loss of the DSB scheme is therefore effectively negligible.

(3) In the 368.49 GHz oxygen absorption band the LSB and USB Jacobians become asymmetric owing to the influence of the 380.20 GHz water-vapour absorption line lying about 12 GHz above it; the DOFS ratio decreased as the IF frequency increased and reached about 0.50–0.55 at IF = 10 GHz. The absolute amount of information lost was larger in the tropical atmosphere than in the subarctic-winter atmosphere, but the fractional loss expressed as a DOFS ratio was comparable in the two atmospheres.

(4) Observations in the 368.49 GHz band improved the retrieval accuracy of temperature, water-vapour VMR and relative humidity mainly below about 13 km in both the subarctic-winter and the tropical atmosphere. Under matched system noise temperature, integration time and total RF bandwidth, the retrieval error of the DD scheme was consistently smaller than that of the DSB scheme, the difference in the ratio of the retrieval error to the prior error reaching at most about 0.28 for temperature in the subarctic-winter atmosphere and about 0.22 in the tropical atmosphere, and at most about 0.10 for relative humidity in the subarctic-winter atmosphere and about 0.19 in the tropical atmosphere.

(5) The relative humidity sensitivity experiments showed that the magnitude of the information loss of the DSB scheme corresponds more clearly to the amount of water vapour in the atmosphere. In the

https://doi.org/10.5194/egusphere-2026-6542
Preprint. Discussion started: 10 November 2026
© Author(s) 2026. CC BY 4.0 License.

tropical atmosphere the difference between the relative humidity retrieval error ratios of the DD and DSB schemes reached about 0.17–0.21 under every saturation condition, about twice the value of about 0.09–0.11 obtained for the subarctic-winter atmosphere. The differences caused by the altitude at which the saturated layer was placed, and by the number of saturated layers, were small in both atmospheres. The advantage of the DD scheme thus corresponds mainly to the absolute amount of water vapour, the differences due to the vertical arrangement of the saturated layers being relatively small.

(6) As an implication for instrument design, the theoretical advantage shown here is guaranteed within the range $\beta \leq 1$ of the system noise temperature ratio. For $\beta > 1$ (the receiver noise temperature of the DD scheme exceeding that of the DSB scheme) the outcome is determined by the balance between the information contained in the difference between the LSB and the USB and the reduction of information caused by the increased noise, and the advantage cannot in general be determined from theory alone. In the numerical experiments the break-even noise temperature ratio β^* at which the DOFS of the DD scheme falls below that of the DSB scheme was about 2.2–2.4 at 368.49 GHz for temperature and for tropical water vapour (about 1.3 for water vapour in the subarctic-winter atmosphere) under the adopted prior, channel and noise assumptions, whereas at 380.20 GHz, whose Jacobians are nearly symmetric, it was about 1.0. In the 368.49 GHz band, therefore, the DD scheme still gives the larger information content even if its system noise temperature is degraded by up to about a factor of two relative to the DSB scheme, except for water vapour in the subarctic-winter atmosphere. Furthermore, although lengthening the integration time can reduce the observation noise, it cannot, for the same fixed DSB channel configuration, recover the information contained in the difference between the LSB and the USB that is lost in the DSB scheme; this information loss is a structural property arising from the symmetry of the Jacobians of the estimated quantities. The adoption of the DD scheme in the 368.49 GHz band should therefore be decided by weighing the system noise temperature that LNA-based receivers, so far demonstrated up to the 300 GHz range, could achieve at 368.49 GHz against the gain in information content brought by the Jacobian asymmetry.

Future work includes the extension to all-weather conditions including ice clouds, a systematic evaluation of the dependence on channel bandwidth, and a comparison of the detection schemes using the noise temperatures of real receivers.

https://doi.org/10.5194/egusphere-2026-6542
Preprint. Discussion started: 10 November 2026
© Author(s) 2026. CC BY 4.0 License.

Appendices

A Loewner order and the diagonal elements of the retrieval error covariance matrix

In Section 2.4 it was shown that the retrieval error covariance matrices of the DD and DSB schemes satisfy

$$\hat{S}_{\mathrm{DD}} \preceq \hat{S}_{\mathrm{DSB}} \tag{A1}$$

Equation (A1) expresses an ordering in the positive semi-definite sense, not an element-by-element inequality between the matrix entries.

Equation (A1) is equivalent to

$$\hat{S}_{\mathrm{DSB}} - \hat{S}_{\mathrm{DD}} \succeq 0 \tag{A2}$$

(Horn and Johnson, 2012), where the symbol $\succeq 0$ indicates that the matrix in question is positive semi-definite. Hence, for an arbitrary vector z,

$$z^{\mathrm{T}}\left(\hat{S}_{\mathrm{DSB}} - \hat{S}_{\mathrm{DD}}\right)z \geq 0 \tag{A3}$$

holds. Rearranging Eq. (A3) gives

$$z^{\mathrm{T}}\hat{S}_{\mathrm{DD}}z \leq z^{\mathrm{T}}\hat{S}_{\mathrm{DSB}}z \tag{A4}$$

We next consider the diagonal elements of the retrieval error covariance matrix. Let e_i denote the standard basis vector whose i-th component is unity and whose other components are zero; then

$$e_i^{\mathrm{T}}\hat{S}e_i = \left[\hat{S}\right]_{ii} \tag{A5}$$

holds. Setting $z = e_i$ in Eq. (A4) yields

$$\left[\hat{S}_{\mathrm{DD}}\right]_{ii} \leq \left[\hat{S}_{\mathrm{DSB}}\right]_{ii} \tag{A6}$$

for every state variable i.

The diagonal elements of the retrieval error covariance matrix are the retrieval error variances of the individual state variables. Equation (A6) therefore shows that the retrieval error variance of each state variable for the DD scheme is no larger than that for the DSB scheme. Moreover, since the square-root function is monotonically increasing over the non-negative range, the retrieval error standard deviations of the individual state variables also satisfy

$$\sqrt{\left[\hat{S}_{\mathrm{DD}}\right]_{ii}} \leq \sqrt{\left[\hat{S}_{\mathrm{DSB}}\right]_{ii}} \tag{A7}$$

The positive semi-definite ordering of Eq. (A1), on the other hand, does not imply that the off-diagonal elements satisfy

$$\left[\hat{S}_{\mathrm{DD}}\right]_{ij} \leq \left[\hat{S}_{\mathrm{DSB}}\right]_{ij},\ i \neq j \tag{A8}$$

The positive semi-definite ordering is an ordering of matrices as a whole, defined through the quadratic form, and not an element-by-element inequality. The off-diagonal elements may therefore individually increase or decrease between the DD and DSB schemes, but the retrieval error variance for any linear combination, and the retrieval error variance of each state variable, are guaranteed to be no larger for the DD scheme than for the DSB scheme.

https://doi.org/10.5194/egusphere-2026-6542
Preprint. Discussion started: 10 November 2026
© Author(s) 2026. CC BY 4.0 License.

B Evaluation method for the relative humidity error

In this study the relative humidity (RH) was not treated as a direct state variable of the MAP retrieval but was computed diagnostically from the temperature and the water-vapour volume mixing ratio (VMR). In order to propagate the retrieval errors of temperature and water-vapour VMR to the relative humidity, the Jacobian of the relative humidity was evaluated by numerical differentiation using finite differences.

B.1 Calculation of relative humidity

The relative humidity (RH) was computed from the temperature, the pressure and the water-vapour volume mixing ratio (VMR), using the saturation vapour pressure given by the Tetens formula (Tetens, 1930). Let the temperature at each altitude be T, the pressure p and the water-vapour VMR q.

The water-vapour partial pressure e is given by

$$e = qp \tag{B1}$$

so that the RH is expressed as

$$RH = 100 \times \frac{e}{e_s(T)} = 100 \times \frac{qp}{e_s(T)} \tag{B2}$$

where $e_s(T)$ is the saturation vapour pressure at the temperature T and the unit of RH is %.

B.2 Saturation vapour pressure from the Tetens formula

The Celsius temperature T_c was obtained from the absolute temperature T as

$$T_c = T - 273.15 \tag{B3}$$

The saturation vapour pressure over water was computed from the Tetens-type formula (Tetens, 1930; Murray, 1967)

$$e_{s,\mathrm{liquid}}(T) = 6.1078 \times 10^{\frac{7.5T_c}{T_c+237.3}} \tag{B4}$$

The saturation vapour pressure over ice was computed from

$$e_{s,\mathrm{ice}}(T) = 6.1078 \times 10^{\frac{9.5T_c}{T_c+265.5}} \tag{B5}$$

The saturation vapour pressures obtained from Eqs. (B4) and (B5) are in hPa.

In this study the saturation vapour pressure over ice was used when the temperature was below 0 °C, and that over water when the temperature was at or above 0 °C. Accordingly,

$$e_s(T) = \begin{cases} e_{s,\mathrm{ice}}(T), & T_c < 0, \\ e_{s,\mathrm{liquid}}(T), & T_c \geq 0 \end{cases} \tag{B6}$$

B.3 Numerical Jacobian of relative humidity

The relative humidity is expressed as a function of the temperature T, the water-vapour VMR q and the pressure p,

$$RH = f(T, q, p) \tag{B7}$$

https://doi.org/10.5194/egusphere-2026-6542
Preprint. Discussion started: 10 November 2026
© Author(s) 2026. CC BY 4.0 License.

The pressure p is here fixed at a known value and its uncertainty is not considered.

The transformation Jacobian of the RH with respect to temperature and water-vapour VMR is defined as

$$G = [G_T \quad G_q] \tag{B8}$$

where

$$G_T = \mathrm{diag}\left(\frac{\partial RH_1}{\partial T_1}, \ldots, \frac{\partial RH_n}{\partial T_n}\right) \tag{B9}$$

and

$$G_q = \mathrm{diag}\left(\frac{\partial RH_1}{\partial q_1}, \ \ldots, \ \frac{\partial RH_n}{\partial q_n}\right) \tag{B10}$$

Since the RH at each altitude is computed solely from the temperature, water-vapour VMR and pressure at that same altitude, G_T and G_q are diagonal matrices.

In this study these partial derivatives were not obtained analytically but were evaluated by numerical differentiation using finite differences. With a central difference, the partial derivative with respect to the temperature at altitude i is computed as

$$\frac{\partial RH_i}{\partial T_i} \simeq \frac{f(T_i+\Delta T_i, q_i, p_i) - f(T_i-\Delta T_i, q_i, p_i)}{2\Delta T_i} \tag{B11}$$

The partial derivative with respect to the water-vapour VMR is computed in the same way as

$$\frac{\partial RH_i}{\partial q_i} \simeq \frac{f(T_i, q_i+\Delta q_i, p_i) - f(T_i, q_i-\Delta q_i, p_i)}{2\Delta q_i} \tag{B12}$$

The G_T and G_q so obtained were applied to the first-order linear error propagation expression given in Appendix B4 to compute the retrieval error covariance matrix and the prior error covariance matrix of RH.

B.4 Propagation of temperature and water-vapour errors into relative humidity

Using the transformation Jacobian defined in B.3, the retrieval errors of temperature and water-vapour VMR were propagated to the retrieval error of RH.

Denoting the retrieval error covariance matrix of the joint state vector of temperature and water-vapour VMR by

$$\hat{S}_x = \begin{bmatrix} \hat{S}_{TT} & \hat{S}_{Tq} \\ \hat{S}_{qT} & \hat{S}_{qq} \end{bmatrix} \tag{B13}$$

the retrieval error covariance matrix of the RH was computed, by first-order linear error propagation, as

$$\hat{S}_{RH} = G\hat{S}_x G^{\mathrm{T}} \tag{B14}$$

Here the cross-covariance of the retrieval errors of temperature and water-vapour VMR arises through the observation. Writing this out block by block gives

$$\begin{aligned} \hat{S}_{RH} = {} & G_T \hat{S}_{TT} G_T^{\mathrm{T}} + G_T \hat{S}_{Tq} G_q^{\mathrm{T}} \\ & + G_q \hat{S}_{qT} G_T^{\mathrm{T}} + G_q \hat{S}_{qq} G_q^{\mathrm{T}} \end{aligned} \tag{B15}$$

The RH retrieval error standard deviation at each altitude i was obtained as

$$\sigma_{RH,i} = \sqrt{\left[\hat{S}_{RH}\right]_{ii}} \tag{B16}$$

https://doi.org/10.5194/egusphere-2026-6542
Preprint. Discussion started: 10 November 2026
© Author(s) 2026. CC BY 4.0 License.

The prior error covariance matrix of the RH was computed in the same way, by applying the same transformation Jacobian to the prior error covariance matrices of the temperature and the water-vapour VMR.

Code and data availability

The analysis code used in this study, together with the configuration files and the numerical output required to reproduce all figures and tables, is available from Zenodo at https://doi.org/10.5281/zenodo.22760420 (Tamura, 2026). The radiative transfer calculations were performed with ARTS version 2.6 (Buehler et al., 2025), which is openly available at https://github.com/atmtools/arts. The atmospheric profiles used are the FASCODE standard atmospheres (Smith et al., 1978) distributed with ARTS.

Author contributions

Ryosuke Tamura conceived the numerical experiments and performed the analysis using the radiative transfer model. Kentaro Araki and Nawo Eguchi advised on the specification of the atmospheric conditions and on the design of the sensitivity experiments, and contributed to the logical structure of the study. Ryosuke Tamura prepared the manuscript with contributions from all co-authors.

Competing interests

The contact author has declared that none of the authors has any competing interests.

Acknowledgements

Artificial intelligence (AI) tools were used during the preparation of this manuscript. ChatGPT (OpenAI) and Claude (Anthropic) were used to assist with code development and to improve the clarity and readability of the manuscript, including its English. All scientific concepts, analyses, interpretations, and conclusions were developed and verified by the authors.

Financial support

This research has been supported by the Japan Society for the Promotion of Science (JSPS) KAKENHI (grant no. JP24K21571).

https://doi.org/10.5194/egusphere-2026-6542
Preprint. Discussion started: 10 November 2026
© Author(s) 2026. CC BY 4.0 License.

References

Barath, F. T., et al.: The Upper Atmosphere Research Satellite Microwave Limb Sounder instrument, J. Geophys. Res., 98, 10751–10762, https://doi.org/10.1029/93JD00798, 1993.

Buehler, S. A., Jiménez, C., Evans, K. F., et al.: A concept for a satellite mission to measure cloud ice water path, ice particle size, and cloud altitude, Q. J. R. Meteorol. Soc., 133, 109 – 128, https://doi.org/10.1002/qj.143, 2007.

Buehler, S. A., Defer, E., Evans, F., Eliasson, S., Mendrok, J., Eriksson, P., Lee, C., Jiménez, C., Prigent, C., Crewell, S., Kasai, Y., Bennartz, R., and Gasiewski, A. J.: Observing ice clouds in the submillimeter spectral range: the CloudIce mission proposal for ESA's Earth Explorer 8, Atmos. Meas. Tech., 5, 1529–1549, https://doi.org/10.5194/amt-5-1529-2012, 2012.

Buehler, S. A., Larsson, R., Lemke, O., Pfreundschuh, S., Brath, M., Adams, I., Fox, S., Roemer, F. E., Czarnecki, P., and Eriksson, P.: The atmospheric radiative transfer simulator ARTS, version 2.6 — Deep python integration, J. Quant. Spectrosc. Radiat. Transf., 341, 109443, https://doi.org/10.1016/j.jqsrt.2025.109443, 2025.

Collard, A. D.: Selection of IASI channels for use in numerical weather prediction, Q. J. R. Meteorol. Soc., 133, 1977–1991, https://doi.org/10.1002/qj.178, 2007.

Comito, C. and Schilke, P.: Reconstructing reality: Strategies for sideband deconvolution, Astron. Astrophys., 395, 357–371, https://doi.org/10.1051/0004-6361:20021277, 2002.

Eriksson, P., Buehler, S. A., Davis, C. P., Emde, C., and Lemke, O.: ARTS, the atmospheric radiative transfer simulator, version 2, J. Quant. Spectrosc. Radiat. Transf., 112, 1551 – 1558, https://doi.org/10.1016/j.jqsrt.2011.03.001, 2011.

Eriksson, P., Rydberg, B., Mattioli, V., Thoss, A., Accadia, C., Klein, U., and Buehler, S. A.: Towards an operational Ice Cloud Imager (ICI) retrieval product, Atmos. Meas. Tech., 13, 53 – 71, https://doi.org/10.5194/amt-13-53-2020, 2020.

Eyre, J. R., Bell, W., Cotton, J., English, S. J., Forsythe, M., Healy, S. B., and Pavelin, E. G.: Assimilation of satellite data in numerical weather prediction. Part II: Recent years, Q. J. R. Meteorol. Soc., 148, 521–556, https://doi.org/10.1002/qj.4228, 2022.

Fox, S., Lee, C., Moyna, B., Philipp, M., Rule, I., Sandford, S., King, R., Oldfield, M., Rea, S., Henry, M., Wang, H., and Harlow, R. C.: ISMAR: an airborne submillimetre radiometer, Atmos. Meas. Tech., 10, 477–490, https://doi.org/10.5194/amt-10-477-2017, 2017.

Goldsmith, P. F.: Quasioptical Systems: Gaussian Beam Quasioptical Propagation and Applications, IEEE Press, New York, 1998.

Gordon, I. E., Rothman, L. S., Hargreaves, R. J., et al.: The HITRAN2020 molecular spectroscopic database, J. Quant. Spectrosc. Radiat. Transf., 277, 107949, https://doi.org/10.1016/j.jqsrt.2021.107949, 2022.

Grützun, V., Buehler, S. A., Kluft, L., Mendrok, J., Brath, M., and Eriksson, P.: All-sky information content analysis for novel passive microwave instruments in the range from 23.8 to 874.4 GHz, Atmos. Meas. Tech., 11, 4217–4237, https://doi.org/10.5194/amt-11-4217-2018, 2018.

Horn, R. A. and Johnson, C. R.: Matrix Analysis, 2nd edn., Cambridge University Press, Cambridge, https://doi.org/10.1017/CBO9781139020411, 2012.

https://doi.org/10.5194/egusphere-2026-6542
Preprint. Discussion started: 10 November 2026
© Author(s) 2026. CC BY 4.0 License.



Janssen, M. A. (Ed.): Atmospheric Remote Sensing by Microwave Radiometry, John Wiley & Sons, New York, 1993.

Kikuchi, K., Nishibori, T., Ochiai, S., et al.: Overview and early results of the Superconducting Submillimeter-Wave Limb-Emission Sounder (SMILES), J. Geophys. Res., 115, D23306, https://doi.org/10.1029/2010JD014379, 2010.

Makarov, D. S., Tretyakov, M. Yu., and Rosenkranz, P. W.: Revision of the 60-GHz atmospheric oxygen absorption band models for practical use, J. Quant. Spectrosc. Radiat. Transf., 243, 106798, https://doi.org/10.1016/j.jqsrt.2019.106798, 2020.

Mlawer, E. J., Payne, V. H., Moncet, J.-L., Delamere, J. S., Alvarado, M. J., and Tobin, D. C.: Development and recent evaluation of the MT_CKD model of continuum absorption, Philos. T. Roy. Soc. A, 370, 2520–2556, https://doi.org/10.1098/rsta.2011.0295, 2012.

Mo, T.: Prelaunch calibration of the Advanced Microwave Sounding Unit-A for NOAA-K, IEEE Trans. Microw. Theory Tech., 44, 1460‑1469, https://doi.org/10.1109/22.536029, 1996.

Murray, F. W.: On the computation of saturation vapor pressure, J. Appl. Meteorol., 6, 203–204, https://doi.org/10.1175/1520-0450(1967)006<0203:OTCOSV>2.0.CO;2, 1967.

Penzias, A. A. and Burrus, C. A.: Millimeter-wavelength radio-astronomy techniques, Annu. Rev. Astron. Astrophys., 11, 51‑72, https://doi.org/10.1146/annurev.aa.11.090173.000411, 1973.

Rabier, F., Fourrié, N., Chafäi, D., and Prunet, P.: Channel selection methods for Infrared Atmospheric Sounding Interferometer radiances, Q. J. R. Meteorol. Soc., 128, 1011 ‑ 1027, https://doi.org/10.1256/0035900021643638, 2002.

Rodgers, C. D.: Characterization and error analysis of profiles retrieved from remote sounding measurements, J. Geophys. Res., 95, 5587‑5595, https://doi.org/10.1029/JD095iD05p05587, 1990.

Rodgers, C. D.: Inverse Methods for Atmospheric Sounding: Theory and Practice, Series on Atmospheric, Oceanic and Planetary Physics, Vol. 2, World Scientific, Singapore, https://doi.org/10.1142/3171, 2000.

Rosenkranz, P. W.: Water vapor microwave continuum absorption: A comparison of measurements and models, Radio Sci., 33, 919‑928, https://doi.org/10.1029/98RS01182, 1998.

Rosenkranz, P. W.: Line-by-line microwave radiative transfer (non-scattering), Remote Sens. Code Library [code], https://doi.org/10.21982/M81013, 2022.

Smith, H. J. P., Dube, D. J., Gardner, M. E., Clough, S. A., Kneizys, F. X., and Rothman, L. S.: FASCODE: Fast Atmospheric Signature Code (Spectral Transmittance and Radiance), Air Force Geophysics Laboratory, Hanscom Air Force Base, Massachusetts, 1978.

Tamura, R.: Analysis code for "Sideband asymmetry determines the information loss of double-sideband detection in submillimetre-wave atmospheric sounding", Zenodo [code], https://doi.org/10.5281/zenodo.22760420, 2026.

Tessmann, A., Leuther, A., Wagner, S., Massler, H., Kuri, M., Stulz, H., Zink, M., Riessle, M., and Merkle, T.: A 300 GHz low-noise amplifier S-MMIC for use in next-generation imaging and communication applications, in: 2017 IEEE MTT-S International Microwave Symposium (IMS), https://doi.org/10.1109/MWSYM.2017.8058687, 2017.

Tetens, O.: Über einige meteorologische Begriffe, Z. Geophys., 6, 297–309, 1930.

https://doi.org/10.5194/egusphere-2026-6542
Preprint. Discussion started: 10 November 2026
© Author(s) 2026. CC BY 4.0 License.



Ulaby, F. T. and Long, D. G.: Microwave Radar and Radiometric Remote Sensing, University of Michigan Press, Ann Arbor, 2014.

Weng, F., Zou, X., Wang, X., Yang, S., and Goldberg, M. D.: Introduction to Suomi National Polar-Orbiting Partnership Advanced Technology Microwave Sounder for numerical weather prediction and tropical cyclone applications, J. Geophys. Res., 117, D19112, https://doi.org/10.1029/2012JD018144, 2012.